Radiation Dose Estimation for Pediatric Patients Undergoing Cardiac Catheterization

by

Chu Wang

Graduate Program in Medical Physics
Duke University

Date:_____

Approved:

_____
Terry Yoshizumi, Supervisor

_____
Joseph Lo, Chair

_____
James Colsher

_____
Rathnayaka Gunasingha

_____
Kevin Hill

Dissertation submitted in partial fulfillment of the requirements for the degree of
Doctor of Philosophy in the Graduate Program in Medical Physics
in the Graduate School of Duke University
2015

ABSTRACT

Radiation Dose Estimation for Pediatric Patients Undergoing Cardiac Catheterization

by

Chu Wang

Graduate Program in Medical Physics
Duke University

Date:_____

Approved:

_____
Terry Yoshizumi, Supervisor

_____
Joseph Lo, Chair

_____
James Colsher

_____
Rathnayaka Gunasingha

_____
Kevin Hill

Dissertation submitted in partial fulfillment of the requirements for the degree of
Doctor of Philosophy in the Graduate Program in Medical Physics
in the Graduate School of Duke University
2015

Abstract

Patients undergoing cardiac catheterization are potentially at risk of radiation-induced health effects from the interventional fluoroscopic X-ray imaging used throughout the clinical procedure. The amount of radiation exposure is highly dependent on the complexity of the procedure and the level of optimization in imaging parameters applied by the clinician. For cardiac catheterization, patient radiation dosimetry, for key organs as well as whole-body effective, is challenging due to the lack of fixed imaging protocols, unlike other common X-ray based imaging modalities.

Pediatric patients are at a greater risk compared to adults due to their greater cellular radio-sensitivities as well as longer remaining life-expectancy following the radiation exposure. In terms of radiation dosimetry, they are often more challenging due to greater variation in body size, which often triggers a wider range of imaging parameters in modern imaging systems with automatic dose rate modulation.

The overall objective of this dissertation was to develop a comprehensive method of radiation dose estimation for pediatric patients undergoing cardiac catheterization. In this dissertation, the research is divided into two main parts: the Physics Component and the Clinical Component. A proof-of-principle study focused on two patient age groups (Newborn and Five-year-old), one popular biplane imaging system, and the clinical practice of two pediatric cardiologists at one large academic medical center.

The Physics Component includes experiments relevant to the physical measurement of patient organ dose using high-sensitivity MOSFET dosimeters placed in anthropomorphic pediatric phantoms.

First, the three-dimensional angular dependence of MOSFET detectors in scatter medium under fluoroscopic irradiation was characterized. A custom-made spherical scatter phantom was used to measure response variations in three-dimensional angular orientations. The results were to be used as angular dependence correction factors for the MOSFET organ dose measurements in the following studies. Minor angular dependence (< ±20% at all angles tested, < ±10% at clinically relevant angles in cardiac catheterization) was observed.

Second, the cardiac dose for common fluoroscopic imaging techniques for pediatric patients in the two age groups was measured. Imaging technique settings with variations of individual key imaging parameters were tested to observe the quantitative effect of imaging optimization or lack thereof. Along with each measurement, the two standard system output indices, the Air Kerma (AK) and Dose-Area Product (DAP), were also recorded and compared to the measured cardiac and skin doses – the lack of correlation between the indices and the organ doses shed light to the substantial limitation of the indices in representing patient radiation dose, at least within the scope of this dissertation.

Third, the effective dose (ED) for Posterior-Anterior and Lateral fluoroscopic imaging techniques for pediatric patients in the two age groups was determined. In addition, the dosimetric effect of removing the anti-scatter grid was studied, for which a factor-of-two ED rate reduction was observed for the imaging techniques.

The Clinical Component involved analytical research to develop a validated retrospective cardiac dose reconstruction formulation and to propose the new Optimization Index which evaluates the level of optimization of the clinician's imaging usage during a procedure; and small sample group of actual procedures were used to demonstrate applicability of these formulations.

In its entirety, the research represents a first-of-its-kind comprehensive approach in radiation dosimetry for pediatric cardiac catheterization; and separately, it is also modular enough that each individual section can serve as study templates for small-scale dosimetric studies of similar purposes. The data collected and algorithmic formulations developed can be of use in areas of personalized patient dosimetry, clinician training, image quality studies and radiation-associated health effect research.

This dissertation is dedicated to

Sulan and Zhenchang

My dear grandparents who taught me the meanings of life and love

&

Jin and Bing

My beloved parents who showed me courage and principles

&

Panpan

My soon-to-be wife, who brightens my day with her smile everyday

Contents

List of Tables

List of Figures

Acknowledgements

I owe my deepest gratitude to my advisor, Dr. Terry Yoshizumi, who is a loving mentor, a supportive friend and a resourceful administrator - a true master in life. My research would not have been possible without the support of Dr. Kevin Hill, whose professionalism and care for children with cardiac conditions are second to none. I owe great appreciations to the rest of my dissertation committee, Drs. James Colsher, Rathnayaka Gunasingha and Joseph Lo, for their guidance and support - all of whom I admire greatly as scientists and model professionals.

I would like to thank Ms. Giao Nguyen of the Duke Radiation Dosimetry Laboratory, for everything she has taught me, helped me and asked me to do.

Sincere thanks are also due to all current and former staff member of the Division of Radiation Safety, especially Mr. Ben Edwards, Mr. Greg Egan, Mr. Dave Jorgenson, Ms. Christine Krieman, Dr. Sue Kurgatt, Ms. Ann Hunter-Paschall, Ms. Netiti Moori, Dr. Robert Reiman, and Ms. Wendy Woehr, for their mentorship and friendship during my everyday work life in the office.

Lastly, I sincerely thank all the (no-longer-new) friends whom I have met during my five-year graduate school career at Duke; special thanks go to Matthew Belley, Yanan Cao, Leo Ding, Natalie Januzis, Brett Mattison, Bria Moore, Justin Raudabaugh, Roland Womack, Zhengzheng Xu, Susu Yan and Yakun Zhang.

Chapter 1. Background and Introduction

1.1 Cardiac catheterization

Cardiac catheterization is a key invasive procedure that helps diagnose and non-surgically treat structural heart defects using specially designed cardiac catheters and implantable devices.[1] In a procedure, a catheter is inserted into the patient's blood vessel in the arm, groin or neck and directed into the heart. Using fluoroscopic X-ray imaging, the clinician is able to see the anatomical structures of the heart and great vessels, identify any abnormalities such as intra-cardiac defects or vascular stenoses, often with the injection of imaging contrast, and perform various interventions with additional implantable devices, such as stents and occlusion devices. In some cases, ultrasound is also used to help navigate the anatomy during the procedure.

Cardiac catheterization has a wide range of applications in cardiology. The main purposes of cardiac catheterization and brief descriptions are listed in Table 1.1. Usually, the more complex the procedure, the longer it takes, the more fluoroscopic imaging is used, and hence, the more radiation dose results in the patient.

Table 1.1 Main purposes and description of cardiac catheterization

Purpose or Name	Description
General Diagnosis	Checking of blood flow, valvular function and other defacts
Biopsy	Removal of a cardiac muscle sample
Balloon Valvuloplasty	Widening of heart valve
Angioplasty	Widening of vessel with balloon
Stent Implementation	Widening of vessel with stent
Balloon and Blade Septostomy	Creation of an unrestricted communication between the upper chamber of the herat
Valve perforation	Opening of blocked pulmonary valve
Occlusion	Plugging up or closing of an unwanted opening

1.2 Fluoroscopic imaging in cardiac catheterization

In modern fluoroscopic imaging systems used in cardiac catheterization, there are two common groups of imaging protocols: a) “Fluoro”, relatively low-dose-rate protocols used to produce low-image-quality live imaging for general purposes such as positioning; and b) “Cine”, relatively high-dose-rate protocols, often assisted with injected contrast agents,used to produce high-image-quality videos for the observation of vascular structures and interventional processes. Within either Fluoro or Cine groups, most modern systems have various dose rate options with different frame rates (15 and 30 frames/second are the two most common).

Aside from the selection of a protocol, clinicians or imaging system operators usually need to input the age, weight and procedure type (body region to be imaged). The system will then use this information to select suitable preset key parameters such as the tube voltage (kVp) and tube current (mA) to ensure a balance of dose and image quality. Additional fine-tuning adjustments of the kVp and mA are done when imaging starts with continuous logical feedback loops to increase or decrease the parameters, to maintain an optimized balance of dose and image quality.

In the imaging system of interest in this dissertation, Allura Xper FD 10/10 (Philips Healthcare, Best, the Netherlands), the kVp and mA presets are a part of the Automatic Dose Rate Control (ADRC) algorithm and a further examination- and patient-type-specific database called the EPX dictates the correct combinations of irradiation parameters, focal spot size, spectral filtration, fluoroscopy type, fluoroscopy dose levels, etc. The entire scheme of automatic exposure modulation and variables are outlined by an Allura Xper-series systems technical note released by Philips[2], and adapted into Table 1.2.

Table 1.2 Variables of ADRC design for cardiac X-ray systems

Control Parameters (Under limits of tube/generator)	Interaction Variables (Under limits of system geometry)	Clinical/Technical Outcomes (IEC Standards, Federal Regulations & local philosophy)
kVp	patient thickness	image quality
beam filtration	contrast detail Z	patient dose
mA	detail thickness	
ms	gantry angle	
detector dose	grid/air gap	
frame rate	scatter/primary	
	source-image distance (SID)	

Fluoroscopic products are regulated by the Food and Drug Administration (FDA), in Article 21CFR1020.32.[3] Pertaining to the contents of this dissertation, all X-ray fluoroscopic equipment in the United States is required to report a dose index called the Air Kerma (AK), which is defined as the air kerma at 15 cm towards the tube from the isocentre for C-arm fluoroscopes, cumulative during the procedure. The position of AK measurement is called the interventional reference point, proposed and implemented by the International Electrotechnical Commission (IEC), to provide an approximate reference location of skin surface at irradiation entrance.[4] For example, during cardiac catheterization for a regular-sized adult patient, the C-arm isocenter is placed at the center of the patient's chest (heart), which is roughly 15 cm away from the skin surface. No special geometrical specification is available for pediatric patients.

In addition to the AK, most modern fluoroscopic systems used for cardiac catheterization in the U.S. report another dose index called the dose-area-product (DAP), which is the product of dose in air and the area of exposure. DAP is the required dose index for fluoroscopic systems in Europe.

The AK and DAP are computed and displayed on the console from look-up tables based on kVp, mA, and beam quality for Philips Allura Xper imaging system. At our institution, the fluoroscopic systems in the pediatric catheterization labs are subject to routine quality assurance services (twice a year) by the Clinical Engineering Department, with assistance from the Philips Healthcare. The service evaluates physics parameters such as tube output and beam quality, such that the accuracy of the AK and DAP are ensured.

1.3 Radiation-associated health risks

X-ray photons, which is what fluoroscopic irradiation really is, is a type of ionizing radiation. By its own naming, ionizing radiation is radiation that has enough energy to ionize an atom by removing electrons from the orbit of the atom. In terms of radiobiological interactions at the cellular level, ionizing radiation may either a) directly ionize the deoxynucleic acid (DNA), or b) ionize the water molecules, creating free radicals such as hydrogen radical (H•) and hydroxyls (OH•), which subsequently interact with the DNA. In both the direct and indirect pathways, DNA can be damaged and mutations can occur. While cells like those of humans do have response

mechanisms such as DNA repair and apoptosis (programmed cell death), ionizing radiation can still damage living cells and result in changes on higher levels than cellular, i.e. organs and organisms.

The radiation-associated health effects of ionizing radiation on humans are classified into two types, stochastic effects and tissue reactions, by the International Commission of Radiological Protection (ICRP).[5,6]

Stochastic Effects

The probability of a stochastic effect, rather than its severity, is a function of radiation dose without threshold. Stochastic effects refer specifically to cancer (solid cancers and leukemia) and hereditary effects. The timeframe of a stochastic effect is long; for example, cancer may take years to develop after a radiation exposure. Therefore, the lifetime-attributable risk of radiation-induced cancer for children is greater than that for adults, as children have a more years of expected life after the exposure. Besides age, the risks of radiation-induced cancer also depend on sex and the tissue/organ in question, due to the different radiosensitivities of different tissue types in the human body. Detailed information on this topic is reported by the National Research Council of the National Academies in the Biological Effects of Ionizing Radiation (BEIR) VII Report.[7]

Tissue Reactions

They are previously known as “deterministic effects” or “non-stochastic effects”. A tissue reaction starts to occur at a certain threshold dose and its severity increases with dose. Notable tissue reactions may include cataract, skin injury and acute radiation sickness. Tissue reactions usually occur from a high “burst” (i.e. high dose in a short time) of radiation exposure, in which case the DNA repair mechanism is not quick enough to repair the large number of DNA damages. Thus, comparing to cancer, the onset of tissue reactions happens rather quickly, from hours to weeks after the radiation exposure.

In diagnostic medical imaging, which involves rather low dose rates, the main concerns of radiation-associated health risks have always been cancer-induction (stochastic effect, long-term risk) and skin injuries (tissue reactions, effects manifest in a short period after exposure, at a threshold of 2 Gy for interventional fluoroscopic irradiation[8]). In recent years, researchers have reported new health risks that are non-cancer, manifest in a long timeframe and at relatively low dose levels.[9-10] Among these newly identified health risks are the risk of radiation-induced cardiovascular diseases. This is going to become another important risk management topic in cardiac catheterization – a procedure that involves primarily the imaging of the heart – as soon as they are better understood. Furthermore, as epidemiological studies are needed to gain a better understanding, follow-up studies on cardiac catheterization patients will

contribute greatly to the topic as well. For any radiation health effect study, dosimetry is one of the fundamental quantities that should be determined.

1.4 Challenges in radiation dose estimation for pediatric patients undergoing cardiac catheterization

When compared to the other common X-ray imaging modalities' recent progression in personalized patient radiation dosimetry, interventional fluoroscopy, particularly pediatric cardiac catheterization, had seen limited success, mainly due to three general challenges. The first challenge is the large variation in patient size, as patient age ranging from 0- to 18-year-old, which is an intrinsic challenge for all pediatric dosimetry studies. The second challenge is the large variation in imaging techniques and parameter settings, such as the automatically-adjusted tube energy and current and the user-determined projection angles and detector distances. This is unique to fluoroscopic procedures. Other modalities such as CT have mostly fixed scan parameters within a protocol, fluoroscopic X-ray used in interventional procedures are used with virtually complete freedom – Clinicians decide on the next imaging techniques and its parameters on the go. Thus, it is very difficult to track all the irradiations applied after a procedure. The third challenge is the limitations of the system output indices as indicators of patient organ dose or whole body effective dose (ED). Using CT as a comparison again, CT's predominantly uniform rotational irradiation likely leads to some degree of correlation between system output (e.g. dose-length product (DLP)) and patient organ dose. However, for fluoroscopy used during

interventional procedures, linear correlation with actual organ- and whole-body doses is less likely for the dose indices (DAP and AK) due to the second challenge just discussed.

These challenges exist at the procedural level, i.e. patient dose for one procedure. Adding to the fact that many patients undergo more than one procedure in a short period of time or over their life-time, the problem, i.e. the estimation of dose and even health risks, becomes ever more challenging.

1.5 Objectives and scope of research

The overall objective of this dissertation is to develop a comprehensive method to estimate radiation dose to pediatric patients undergoing cardiac catheterization. Such results will not only be beneficial for dosimetry alone. It can also provide important quantitative information for optimized imaging usage, so that the clinicians can optimize image quality with respect to dose.

This proof-of-principle study focused on two patient age groups (the Newborn and Five-year-old), one popular biplane imaging system (Allura Xper FD 10/10), and the clinical practice of two pediatric cardiologists at one large academic medical center. In this dissertation, the research is separated into two main parts: a Physics Component and a Clinical Component.

The Physics Component (Chapters 2-4) includes experiments relevant to the physical measurement of patient organ dose using high-sensitivity metal-oxide semiconductor field-effect transistor (MOSFET) dosimeters (Model: TN-1002-RDH; Best

Medical Canada, Ottawa, Canada) placed in anthropomorphic pediatric phantoms (Model 703 for Newborn and Model 705 for Five-year-old; CIRS, Norfolk, Virginia).

In Chapter 2, the three-dimensional angular dependence of MOSFET detectors in scatter medium under fluoroscopic irradiation was characterized. A custom-made spherical scatter phantom was used to measure response variations in three-dimensional angular orientations. The results are used as angular dependence correction factors for the MOSFET organ dose measurements for the studies in Chapters 3 and 4.

In Chapter 3, the cardiac dose for common fluoroscopic imaging techniques for pediatric patients in the two age groups was measured. Imaging with variations of individual key imaging parameters were performed to observe the quantitative effect of imaging optimization or lack thereof. Along with each measurement, the two radiation indices, the AK and DAP, were recorded and compared to the measured cardiac and skin doses.

In Chapter 4, the effective dose for Posterior-Anterior and Lateral fluoroscopic imaging techniques for pediatric patients in the two age groups was determined. The effect on dose of removing the anti-scatter grid was also studied.

The Clinical Component (Chapter 5) includes analytical research to develop a dose reconstruction method, using the data collected in the Physics Component and actual procedure records performed on the biplane X-ray imaging system at Duke University Medical Center. In addition, a new imaging optimization index was

proposed and experimented with real clinical data to help clinicians track their imaging usage in a convenient, intuitive way.

In Chapter 6, the dissertation is concluded with summarized limitations and results, proposed applications as well as general future outlook.

Part I: Physics Component

Chapter 2. Characterization of MOSFET dosimeter angular response using a spherical phantom for fluoroscopic dosimetry

2.1 Introduction

MOSFET dosimeters, placed in anthropomorphic phantoms, are becoming a standard method for organ dosimetry in medical X-ray imaging applications. In these dosimetric scenarios, MOSFET's key advantage is its fast, near-real-time reading capability. On the other hand, MOSFET's angular dependence, due to its non-isotropic physical configuration, presents a challenge whenever the irradiation geometry is such that the detector active area is not perpendicular to the X-ray beam.

Fluoroscopy procedures, for diagnostic or interventional purposes, often involve a collection of imaging projection angles. Therefore, it is necessary to characterize the dosimeter's angular response to ensure the MOSFET's dosimetric accuracy. Studies have been conducted to characterize MOSFET dosimeters' angular dependence under X-ray irradiation using various dosimeter models, beam qualities and scatter media, for their respective purposes.[11-14] However no studies have looked specifically at MOSFET angular dependence when used to quantify radiation dose from cardiac catheterization.

The goal of our study was to characterize the dosimeter's angular response in the fluoroscopic irradiation involved in pediatric cardiac catheterization procedures.

2.2 Materials and methods

2.2.1 Beam quality

At our institution, most cardiac catheterization procedures on pediatric patients are performed using a Philips Allura FD10/10, a biplane X-ray fluoroscopy system. Like most modern fluoroscopy systems, this particular system automatically modulates the X-ray energy (kV) and current (mA) for different patient sizes or attenuation thickness, in order to achieve an optimal balance between image quality and patient dose. In this study, we concentrated on the beam quality for young pediatric patients (≤ 5 years of age) as these patients are at increased risk of long-term harmful effects related to radiation exposure, and because younger patients often undergo prolonged procedures involving relatively higher radiation doses. By using a Newborn and a Five-year-old anthropomorphic phantom as clinical simulations on the system, the peak energy was found to be around 70kV and the applied filtration was 0.4mm Cu + 1.0mm Al. Spekcalc (Windows Release 1.1)[15-17], a photon spectrum simulation software, estimated the first Half-Value Layer (HVL) to be 5.81 mm Al for such an X-ray beam.

A biological X-ray irradiator, X-Rad 320 (PXI, North Branford, Connecticut), was used to simulate the clinical beam quality, with peak energy of 70kV and filtration of 0.5mm Cu. The first HVL was directly measured by the Piranha (RTI Electronics, Mölndal, Sweden), a multi-purpose X-ray QA meter, to be 6.45mm Al.

2.2.2 MOSFET Dosimeter

The main component of a MOSFET detector consists of two MOSFETs fabricated on a silicon rectangle encapsulated with epoxy resin. The active area of detection is 0.2 mm x 0.2 mm. A more detailed description of the rationale of operations of the dosimeter can be found in a prior thesis work by Wang.[18] The asymmetry of geometrical configuration of MOSFET dosimeters makes them intrinsically susceptible to angular dependence in certain irradiation situations.

The MOSFET dosimeter of interest is the high-sensitivity MOSFET. The dosimeter response was read by a reader unit (TN-RD-60; Best Medical Canada) and dedicated software (TN-RD-49; Best Medical Canada) on a laptop computer. The bias supply setting was set at "High", as for actual clinical dosimetry scenarios, for best accuracy.

2.2.3 Phantom and irradiation setup

A custom-made acrylic spherical phantom was used as the scatter medium. (Figure 2.1) The phantom contained a sphere (4" diameter) sitting on top of a square holder (2" sides, 1" height) with a concave top – the sphere is free to rotate in any axis on the holder. There are two straight holes, with 3mm and 1mm diameters respectively, on the surface drilled straight to the center of the sphere for detector placement. In this study a single MOSFET dosimeter was placed in the larger-diameter hole.

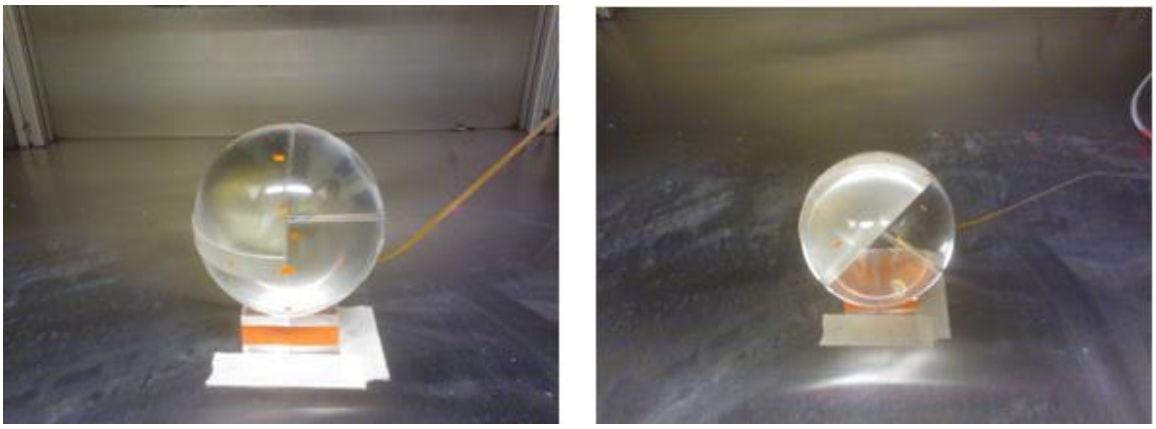

Figure 2.1 Spherical phantom with MOSFET inserted in two different angular orientations. The orange stickers on the phantom surface mark various angular references.

2.2.4 Angular response measurements

First, dosimeter response (in mV) was measured in two rotational axes, axial (ψ) and normal-to-axial (ϑ), in 30° increments (Figure 2.2).

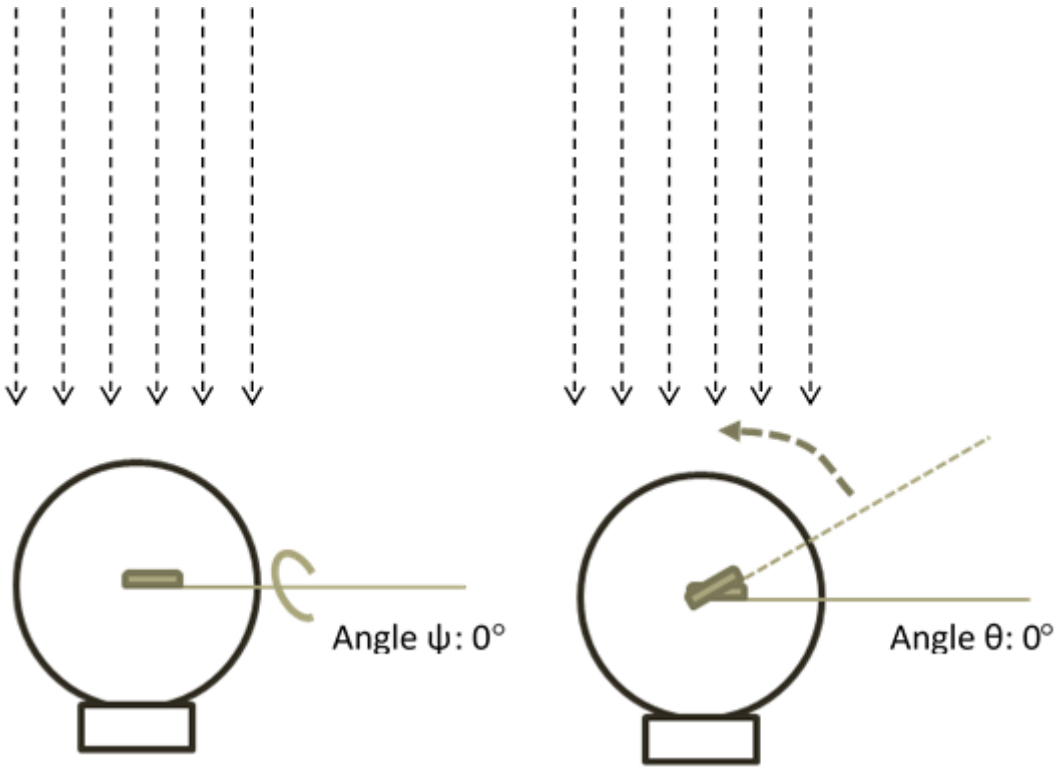

Figure 2.2 Schematic drawing of angular response measurements in (left) axial and (right) normal-to-axial rotations. A single MOSFET dosimeter is placed in the center of the spherical phantom, under X-ray irradiation directly above. The reference angle (ψ=0°, ϑ=0°) is at when the detector epoxy is perpendicular to the incoming beam.

Second, five projection angles commonly used in pediatric cardiac catheterization were tested. In their clinical naming convention the projections were: a) Posterior-Anterior (PA); b) Lateral; c) 70° LAO/ 20° Cranial; d) 20° LAO/ 15° Cranial; and e) 30° RAO. Their corresponding ψ and ϑ angles are listed in Table 2.1. As the first three clinically relevant angles are included in the axial and normal-to-axial measurements, additional dosimeter responses were measured for the latter two angles.

For both measurement groups mentioned above, at every angle, three MOSFET dosimeters (usage level ~3000 mV) were each exposed for 1 min, repeated three times; the average detector response was normalized to the reference angle where the dosimeter epoxy is perpendicular to the beam (ψ=0°, ϑ=0°), which was also the PA projection angle in the clinical setup.

2.3 Results

Normalized angular responses in the axial and normal-to-axial rotations (ψ and ϑ angles, respectively) are shown in Figure 2.3. In the axial rotation, the MOSFETs displayed minimal angular dependence, within 10% deviation in relative response from the reference angle (ψ=0°, ϑ=0°) for all measured angles (Figure 2.3 (left)). In the normal-to-axial rotation, similar minimal angular dependence was observed for all measured angles except for the θ=270° angle, which had 83% relative response (Figure 2.3 (right)).

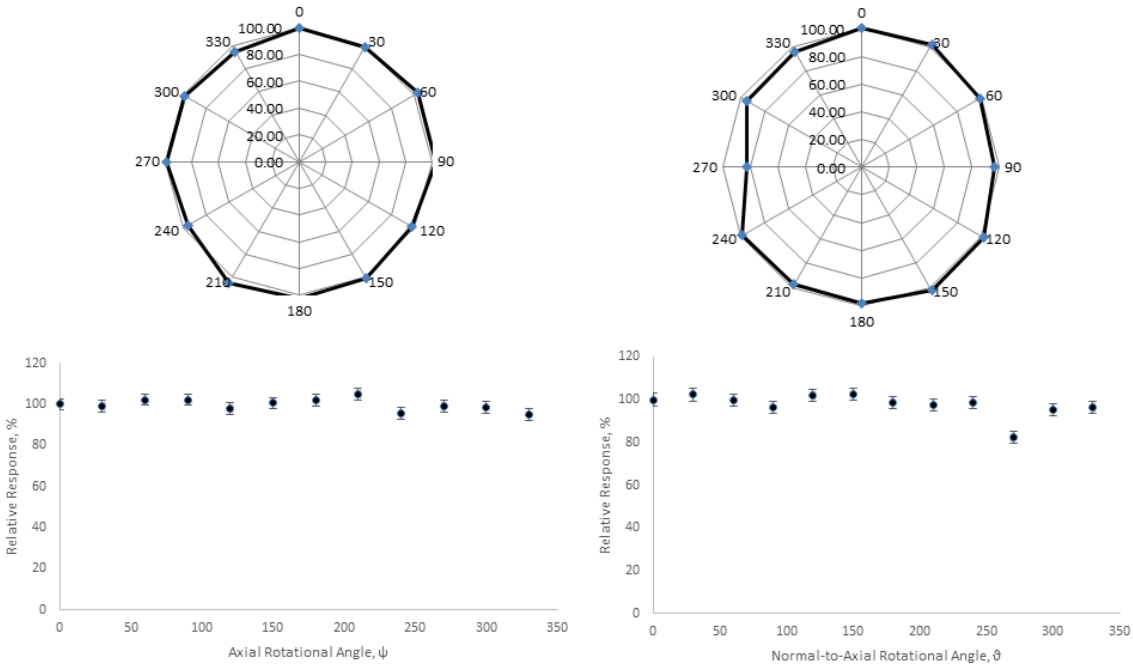

Figure 2.3 Normalized angular response in the (left) axial and (right) normal-to-axial rotations.

At the five clinically relevant oblique angles, the relative angular response was measured to be all within 10% deviation from the reference angle (Table 1).

Table 2.1: Spherical coordinates of the five clinically relevant angles and their respective measured relative angular response (±1σ).

Clinically Relevant Angles	ψ	ϑ	Relative Angular Response (%)
PA	0°	0°	100 ± 3
Lateral	90°	0°	102 ± 3
70°LAO/20°Cranial	70°	340°	90 ± 3
20°LAO/15°Cranial	20°	345°	92 ± 3
30°RAO	330°	0°	95 ± 3

2.4 Discussion

Overall, with the irradiation parameters of our experiment, the results show that there is no significant angular dependence for the TN-1002RDH MOSFET dosimeters. Particularly for the targeted application of pediatric cardiac catheterization dosimetry, the dosimeters showed minimal angular dependence at all five clinically relevant projections angles.

As the MOSFET technology becomes more popular in medical imaging dosimetry, the characterization of angular dependence presents unique challenges for different modalities and irradiation parameters. Dong et al[19] conducted free-in-air measurements at normal-to-axial rotation under 60, 90, 117 kVp irradiation for TN-1002RDI dosimeters for conventional radiography. They reported considerable under-response (less than 80%) at the 90° and 270° angles. Pomjie et al[20] conducted free-in-air and cylinder-phantom measurements at normal-to-axial rotation under 60, 90, 120 kVp irradiation for TN-1002RDH dosimeters for conventional radiography. The presence of different scatter media of air, soft-tissue-, lung- and bone-equivalent materials led to various angular response behaviors. More recently, Koivisto[21] et al conducted free-in-air and cylindrical-phantom measurements at axial, normal-to-axial and tangent-to-axial rotations under 80 kVp irradiation for TN-1002RDH dosimeters for CT. In their findings, for free-in-air, the most significant under-response occurred at the 90° and 270° angles in

normal-to-axial rotations, at less than 60% relative response; for acrylic phantoms, the dosimeter response became less angular dependent.

The results of these studies, including ours, can be compared in complete parallel due to the varying beam qualities involved. However, it can be reasoned that the 90° and 270° angles in normal-to-axial rotation (ϑ) are susceptible to relative under-response, likely because at these two angles, the dosimeter is parallel to the incoming beam, with the smallest active-region cross section facing the direct irradiation. It is possible that the lack of angular dependence at 90 degrees and the overall lower degree of angular dependence in our study might be attributable to the phantom as a scatter medium and the relative low X-ray energy. The presence of phantoms leads to more scatter photons, thus "smoothing out" the potential angular response at different angles, as compared to a free-in-air exposure; and theoretically, the role of the scatter photons is more significant with lower energy and softer X-ray as well as more attenuation by the phantom (larger size and denser material).

From a practical perspective, in certain dosimetry experiments, the angular response correction can be as important as the energy calibration. As the MOSFET has a sensitive energy response, an angular response measurement must be carefully designed so that the beam quality and scatter medium match well with the actual dosimetry experiment. Reassuringly, for the purposes of dosimetry related to pediatric cardiac catheterization, our study demonstrated relatively little angular dependence when

applied to typical camera projections used during these procedures. However one needs to be careful when directly comparing angular dependence studies with different methods and for different clinical applications. The discrepancies between our data and those previously reported suggest that investigators should consider angular dependence studies tailored to the clinical application of interest.

Meanwhile, we acknowledge three main limitations of our approach. First, the difference in scatter medium: the spherical phantom used in the angular dependence measurements in this study is not a perfect representation for the pediatric anthropomorphic phantoms used in the dosimetry studies or the actual patient. However, because of the three-dimensionality of the variation in projection angles, a spherical acrylic phantom is a practical solution for angular response measurement. In addition, the size of the phantom (4" diameter) approximately matches the size of the chest region (with consideration for the low-density lungs) of a small child. Second, individual variation in dosimeter response is always a source of error in MOSFET dosimeter measures. To reduce the variability, the average response of three dosimeters was calculated and used. Third, MOSFET dosimeters tend to have greater instability in response with increasing usage (in mV). For this reason, all three dosimeters used were at ~3000 mV in usage at the beginning of this study – generally dosimeters are considered not suitable for measurement if dosimeter usage exceeds ~15,000 mV [22] – to represent a more realistic experimental scenario.

2.5 Conclusions

To the best of our knowledge this is the first study addressing MOSFET angular response characteristics in the fluoroscopic environment. We measured the angular response of a popular high-sensitivity MOSFET dosimeter, at angles in both general rotational axes as well as common clinically relevant projection angles used in pediatric cardiac catheterization. In the next Chapter, the relative angular responses will be applied as angular correction factors for experiments in pediatric cardiac catheterization dosimetry. The custom-designed spherical phantom may be useful for future angular dependence characterization studies, especially for multi-dimensional oblique projection angles used in interventional fluoroscopy.

Chapter 3. Cardiac and skin dose measurement using anthropomorphic phantoms

3.1 Introduction

The frequent use of interventional fluoroscopic imaging during a cardiac catheterization procedure, often results in considerable radiation exposure to the patient. Children represent a major portion of the patient population undergoing cardiac catheterization largely for those patients with congenital heart diseases.[23] At the same time, children are at a greater risk than adults of radiation-associated health effects because of their faster-growing cells and longer remaining life expectancy.[24]

Clinical groups and government agencies have dedicated effort to study and report patient radiation dose from cardiac catheterization.[25-40] By the Joint Commission's requirements, any peak skin dose exceeding 15 Gy from fluoroscopy-guided procedures is a sentinel event. The common motivation in these studies was the concern of skin injury and the common goal was to find methods for dose reduction.

On the other hand, the reported irradiation output-related quantities in these studies are predominantly limited to fluoro time, DAP and AK, all of which are quantities that are better-suited to represent how much irradiation was used, rather than how much radiation dose the patient actually received. Therefore, there is still a real need to conduct dosimetric research to determine dose in individual organs, internal and surface.

Our MOSFET-phantom approach, has become a standard method in patient organ dose measurements in various diagnostic X-ray imaging modalities.[41 42] Using anthropomorphic phantoms to simulate the patient and small MOSFET dosimeters placed inside the phantom at the organs of interest, the method is also suitable to our need for cardiac catheterization dosimetry.

In this study, the organs of interest were the skin and heart: Skin for reasons stated above; and heart, as a representative internal organ which is at the approximate geometric center of the chest and also for the potential dosimetric application in radiation-associated cardiovascular diseases research.

The purpose of this study was three-fold: 1) to directly measure the cardiac and skin entrance dose rate for the five most common imaging projection angles, at standard, optimized parameter settings; 2) to evaluate the quantitative effect in patient radiation dose with non-optimized imaging parameters; and 3) to evaluate the efficacy of the dose indices, DAP and AK, as good indicators of patient dose.

3.2 Materials and Methods

3.2.1 Imaging System

All imaging was performed using the Philips Allura Xper FD 10/10, a biplane X-ray imaging system. It has two imaging arches, namely the "C-arm" (based on the floor) and "G-arm" (based off the ceiling) by the manufacturer's convention. Both the C-arm

and G-arm are equipped with identical X-ray tubes and square 10-inch diagonal flat-panel detectors. Three magnification levels are available: 6-, 8- and 10-inch diagonal.

As introduced in Chapter 1, the system automatically modulates the irradiation parameters, kVp and mA, per their ADRC system and EPX database, the latter of which is specially configured for the pediatric cardiac catheterization lab and its procedures (the rationale and configuration of the EPX database is confidential information of the manufacturer and is not available to the author).

Notably, the ADRC has a "Patient Type" setting, which dictates different kVp- and mA- curves for different patient sizes, see Table 3.1. This is one of the critical operator-defined settings that would make a significant effect on dose rate and is relevant to the error-scenario measurements introduced in Section 3.2.5 later.

Table 3.1 "Patient Type" selections of the Allura Xper FD 10/10 system

#	**Patient Type**	**Relevance to this study**
1	Baby < 5 kg	Suitable for Newborn
2	Child 5-15 kg	
3	Child 15-40 kg	Suitable for Five-year-old
4	Very Small 40-55 kg	
5	Small 55-70 kg	
6	Normal 70-90 kg	
7	Large > 90 kg	

3.2.2 Anthropomorphic phantoms

The Atom-series Newborn and Five-year-old anthropomorphic phantoms were used to simulate patients in the respective age groups. Their specifications are listed in Table 3.2.

Table 3.2 Phantom specifications

	Newborn	Five-year-old
Height	51 cm	110 cm
Weight	3.5 kg	19 kg
Thorax Dimensions	9 x 10.5 cm	14 x 17 cm
Physical Density	1.41 g/cc	1.52 g/cc
Electron Density	4.498×10^{23} electron/cc	4.801×10^{23} electron/cc
Arms	Yes	No

The experimental setup, with the MOSFET-loaded phantom lying on the patient bed of the imaging system, is shown in Figure 3.1.

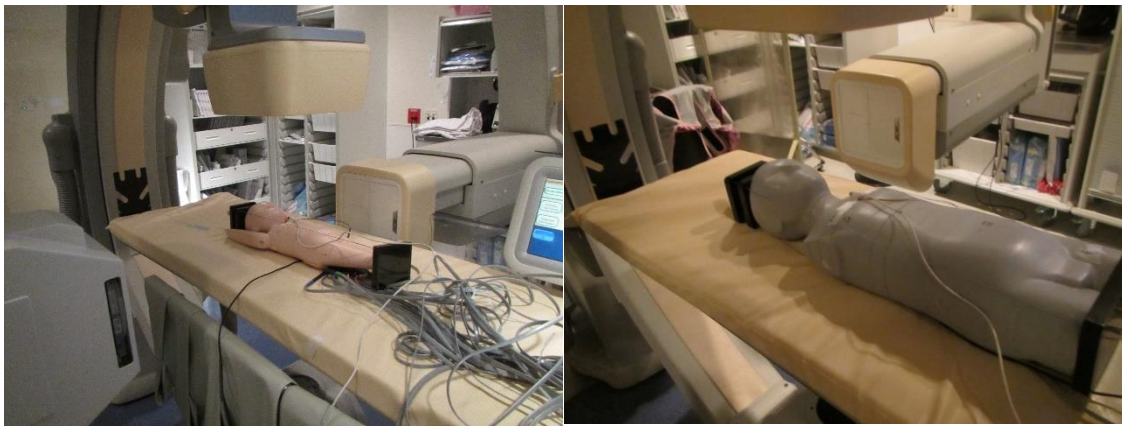

Figure 3.1 Experimental setup. Left: Newborn; Right: Five-year-old

3.2.3 Dosimeter placement

High-sensitivity MOSFET dosimeters and 0.18cc ionization chambers (Radcal, Monrovia, CA) were used to measure the cardiac and skin doses, respectively.

For the Newborn, one MOSFET dosimeter was placed in the center of the heart, measuring the estimated average heart dose. Figure 3.2 shows location of the custom-drilled dosimeter hole in Slab #7 of the Newborn phantom. Two MOSFET dosimeters were placed on the skin surfaces at radiation entrance and exit, in the central area of the FOV: The positions depended on the projection angle; i.e. for PA, they are placed at center chest and center upper back, for LAT, on both sides of the chest, and so on.

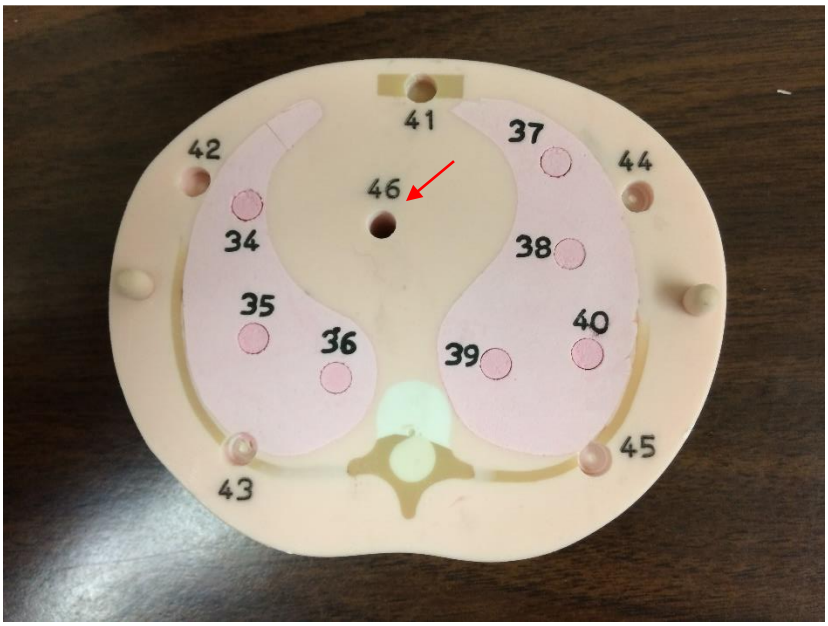

Figure 3.2 Slab #7 of the Newborn phantom. Red arrow indicates the location of the dosimeter placement

For the Five-year-old, five MOSFET dosimeters were employed, measuring the estimated average heart dose as well as doses at various distinctive anatomical locations

(Table 3.3). Figure 3.3 shows the location of the custom-drilled dosimeter hole in Slab #7 of the Newborn phantom. Two ionization chambers were placed on the skin surfaces at radiation entrance and exit, in the central area of the FOV, in the same fashion as in the Newborn skin dosimeter placements.

Table 3.3: Dosimeter holes and their corresponding cardiac anatomic structures

Dosimeter Holes	Cardiac anatomical structures
H10	Approximate geometric center of the heart
H11	Right Coronary Artery / Tricuspid Valve / Pulmonary Valve
H12	Circumflex Artery / Mitral Valve
H13	Distal Right Coronary Artery / Tricuspid Valve
H14	Left Anterior Descending Artery / Interventricular Septum

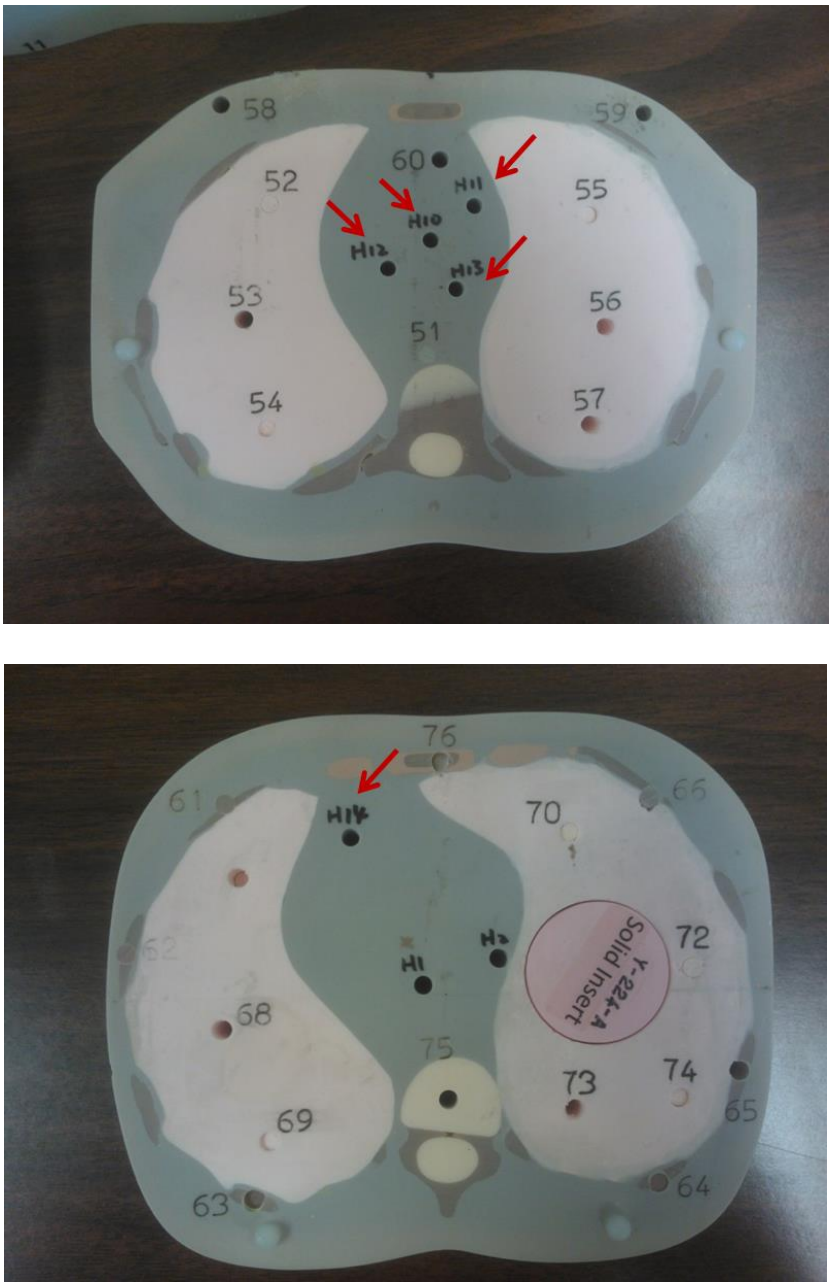

Figure 3.3 Slabs #12 (top) and #13 (bottom) of the Five-year-old phantom. Black marker-numberings and red arrows indicates the locations of the dosimeter placement

All MOSFET dosimeter were placed with the epoxy facing toward the posterior of the phantom. Dosimeter angular response correction factors (from Chapter 2) were

applied to correct for the respective angular orientations of the incoming radiation in different imaging projection angles.

For all imaging techniques studied, dosimeters were read after at least 300 seconds for Fluoro and 60 seconds for Cine, in order to accumulate enough energy deposition to ensure accurate dosimeter readings. Each imaging technique was repeated at least twice and the average measured organ doses were calculated. All dose values were then normalized to dose rates, in units of mGy/s.

3.2.4 Imaging Protocols and Techniques

For convenience and clarity, a particular combination of imaging parameters was defined as an imaging technique. With the variations in individual parameters, there are virtually an infinite number of possible techniques. It is easy to appreciate that the high degree of freedom in imaging parameters as a unique problem in dosimetry for fluoroscopy compared to other modalities. Therefore, upon consultation with a pediatric cardiologist of 10 years of experience and a regular user with the imaging system of interest, nine Fluoro and nine Cine techniques for each age group, have been defined as the representative imaging techniques. The parameters of all techniques are listed in Table 3.4 and explained in the following paragraphs.

All techniques are in 15 f/s, the dosimetry of like techniques in other frame rates can easily be scaled if needed. The common filtration is 0.4mm Cu + 1mm Al.

In each set of 9 techniques (Fluoro or Cine), Technique #1-5 represented the five commonly used projection angles (as introduced in Section 2.2.4), at standard optimized settings. Technique #6-9 were techniques with individual non-optimized parameters: Technique #6 used an increased Source-to-Image Distance (SID); Techniques #7-8 used the other magnification levels (note the standard magnification is 6″ and 8″ for the Newborn and the Five-year-old, respectively); and Technique #9 with no collimation (10″ diagonal square, as compared to 7.7″ diagonal square standard collimation).

For the Newborn group in particular, Technique #2 had two variations, with the phantom arms raised up by the head (#2a) and down by the torso (#2b). By measuring the radiation dose with varying specific parameters while controlling the others, a quantitative dosimetric understanding of the imaging optimization could be obtained.

Table 3.4 Representative imaging techniques, under correct Patient Type settings. a) Newborn, Fluoro; b) Newborn, Fluoro; c) Five-year-old, Fluoro; and d) Five-year-old, Cine

a) Newborn, Fluoro, Patient Type: "Baby < 10 lb"								
Technique	**C/G-arm**	**kV**	**mA**	**Projection Angle**	**Frame/s**	**SID (cm)**	**Magnification**	**Collimation**
Fluoro#1 PA 6" w/ coll.	C-arm	65	2.2	0/0 (PA)	15	93	6"	Yes
Fluoro #2a LAT (Arms-up)	G-arm	65	2.1	90LAO/0 (Lateral)	15	112	6"	Yes
Fluoro #2b LAT (Arms-down)	G-arm	71	3.5	90LAO/0 (Lateral)	15	112	6"	Yes
Fluoro#3 70/20	G-arm	66	2.4	70LAO/20Cranial	15	108	6"	Yes
Fluoro#4 20/15	C-arm	65	2.1	20LAO/15Cranial	15	93	6"	Yes
Fluoro#5 30 RAO	C-arm	66	2.3	30RAO/0Caudal	15	93	6"	Yes
Fluoro#6 High SID	C-arm	68	2.8	0/0 (PA)	15	113	6"	Yes
Fluoro#7 8"	C-arm	64	1.9	0/0 (PA)	15	93	8"	Yes
Fluoro#8 10"	C-arm	62	1.4	0/0 (PA)	15	93	10"	Yes
Fluoro#9 w/o coll.	C-arm	69	2.2	0/0 (PA)	15	93	6"	No

b) Newborn, Cine, Patient Type: “Baby < 10 lb”								
Technique	**C/G-arm**	**kV**	**mA**	**Projection Angle**	**Frame/s**	**SID (cm)**	**Magnification**	**Collimation**
Cine#1 PA 6" w/ coll.	C-arm	69	118	0/0	15	93	6"	Yes
Cine#2a LAT (Arms-up)	G-arm	69	117	90LAO/0 (Lateral)	15	112	6"	Yes
Cine#2b LAT (Arms-down)	G-arm	75	164	90LAO/0 (Lateral)	15	112	6"	Yes
Cine#3 70/20	G-arm	70	128	70LAO/20Cranial	15	108	6"	Yes
Cine#4 20/15	C-arm	75	166	20LAO/15Cranial	15	93	6"	Yes
Cine#5 30 RAO	C-arm	69	119	30RAO/0Caudal	15	93	6"	Yes
Cine#6 High SID	C-arm	72	140	0/0	15	113	6"	Yes
Cine#7 8"	C-arm	67	106	0/0	15	93	8"	Yes
Cine#8 10"	C-arm	65	88	0/0	15	93	10"	Yes
Cine#9 w/o coll.	C-arm	76	123	0/0	15	93	6"	no

Five-year-old, Fluoro, Patient Type: "Child 35 – 90 lb"								
Technique	**C/G-arm**	**kV**	**mA**	**Projection Angle**	**Frame/s**	**SID (cm)**	**Magnification**	**Collimation**
Fluoro#1 PA 8" w/ coll.	C-arm	74	4.6	0/0 (PA)	15	100	8"	Yes
Fluoro #2 LAT	G-arm	71	3.5	90LAO/0 (LAT)	15	112	8"	Yes
Fluoro#3 70/20	G-arm	71	3.5	70LAO/20Cranial	15	112	8"	Yes
Fluoro#4 20/15	C-arm	76	4.8	20LAO/10Cranial	15	100	8"	Yes
Fluoro#5 30 RAO	C-arm	72	4.0	30RAO/0	15	100	8"	Yes
Fluoro#6 High SID	C-arm	78	5.4	0/0 (PA)	15	120	8"	Yes
Fluoro#7 6"	C-arm	77	5.3	0/0 (PA)	15	100	6"	Yes
Fluoro#8 10"	C-arm	70	3.5	0/0 (PA)	15	100	10"	Yes
Fluoro#9 w/o coll.	C-arm	74	4.5	0/0 (PA)	15	100	8"	No

Five-year-old, Cine, Patient Type: "Child 35 – 90 lb"								
Technique	**C/G-arm**	**kV**	**mA**	**Projection Angle**	**Frame/s**	**SID (cm)**	**Magnification**	**Collimation**
Cine#1 PA 8" w/ coll.	C-arm	65	318	0/0	15	100	8"	Yes
Cine#2 LAT	G-arm	62	213	90LAO/0	15	112	8"	Yes
Cine#3 70/20	G-arm	62	210	70LAO/20Cranial	15	112	8"	Yes
Cine#4 20/15	C-arm	65	354	20LAO/10Cranial	15	100	8"	Yes
Cine#5 30 RAO	C-arm	63	252	30RAO/0	15	100	8"	Yes
Cine#6 High SID	C-arm	66	395	0/0	15	120	8"	Yes
Cine#7 6"	C-arm	66	383	0/0	15	100	6"	Yes
Cine#8 10"	C-arm	63	230	0/0	15	100	10"	Yes
Cine#9 w/o coll.	C-arm	64	311	0/0	15	100	8"	No

3.2.5 Operator-error scenario: cardiac dose measurements using an incorrect patient size setting

A possible operator-error scenario was simulated for the Newborn, where the Patient Type setting was incorrectly "ignored" at the default "Child 35 – 90 lb". It meant

that the 10 lb Newborn would be under imaging irradiation suitable for a much bigger child, by the ADRC and XPS modulations. All nine Fluoro and Cine imaging techniques were tested, their parameters are shown in the Table 3.5 below.

Table 3.5 Representative imaging techniques, under incorrect Patient Type settings. a) Newborn, Fluoro; b) Newborn, Fluoro

a) Newborn, Fluoro, Patient Size: "Child 35 – 90 lb"								
Technique	**C/G-arm**	**kV**	**mA**	**Projection Angle**	**Frame/s**	**SID (cm)**	**Magnification**	**Collimation**
Fluoro#1 PA 6" w/ coll.	C-arm	69	3.3	0/0 (PA)	15	93	6"	Yes
Fluoro #2a LAT (Arms-up)	G-arm	66	2.4	90LAO/0 (Lateral)	15	112	6"	Yes
Fluoro #2b LAT (Arms-down)	G-arm	73	4.1	90LAO/0 (Lateral)	15	112	6"	Yes
Fluoro#3 70/20	G-arm	70	3.2	70LAO/20Cranial	15	108	6"	Yes
Fluoro#4 20/15	C-arm	68	2.8	20LAO/15Cranial	15	93	6"	Yes
Fluoro#5 30 RAO	C-arm	67	2.6	30RAO/0Caudal	15	93	6"	Yes
Fluoro#6 High SID	C-arm	74	4.4	0/0 (PA)	15	113	6"	Yes
Fluoro#7 6"	C-arm	67	2.8	0/0 (PA)	15	93	8"	Yes
Fluoro#8 10"	C-arm	64	1.9	0/0 (PA)	15	93	10"	Yes
Fluoro#9 w/o coll.	C-arm	69	3.3	0/0 (PA)	15	93	6"	No

b) Newborn, Cine, Patient Size: "Child 35 – 90 lb"								
Technique	**C/G-arm**	**kV**	**mA**	**Projection Angle**	**Frame/s**	**SID (cm)**	**Magnification**	**Collimation**
Fluoro#1 PA 6" w/ coll.	C-arm	74	153	0/0	15	93	6"	Yes
Fluoro #2a LAT (Arms-up)	G-arm	70	124	90LAO/0 (Lateral)	15	112	6"	Yes
Fluoro #2b LAT (Arms-down)	G-arm	77	178	90LAO/0 (Lateral)	15	112	6"	Yes
Fluoro#3 70/20	G-arm	63	238	70LAO/20Cranial	15	108	6"	Yes
Fluoro#4 20/15	C-arm	62	202	20LAO/15Cranial	15	93	6"	Yes
Fluoro#5 30 RAO	C-arm	62	185	30RAO/0Caudal	15	93	6"	Yes
Fluoro#6 High SID	C-arm	78	186	0/0	15	113	6"	Yes
Fluoro#7 6"	C-arm	71	131	0/0	15	93	8"	Yes
Fluoro#8 10"	C-arm	67	105	0/0	15	93	10"	Yes
Fluoro#9 w/o coll.	C-arm	73	150	0/0	15	93	6"	no

3.3 Results

(All relevant numerical data are included in Appendix A.)

The measured cardiac and skin entrance dose rates for the Newborn and Five-year-old, for all nine Fluoro and nine Cine imaging techniques, at correct and incorrect Patient Type settings, were presented in Figures 3.4 and 3.5, respectively.

Under correct Patient Type settings, for the standard imaging techniques at the five projection angles (Technique #1-5), the cardiac (center of the heart) dose rates were measured to be 0.0066 – 0.024 mGy/s for Fluoro and 0.027 – 0.051 mGy/s for Cine for the Newborn and 0.014 – 0.027 mGy/s for Fluoro and 0.093 – 0.20 mGy/s for Cine for the Five-year-old; the skin entrance dose rates were measured to be 0.020 – 0.040mGy/s for

Fluoro and 0.080 – 0.10 mGy/s for Cine for the Newborn and 0.047 – 0.083 mGy/s for Fluoro and 0.67 – 1.3 mGy/s for Cine for the Five-year-old.

Quantitative dose rate effects in terms of imaging parameter optimization were obtained as well (Techniques #6-10). Technique #6: Increasing the SID by 20cm, from 93cm to 113cm for the Newborn and from 100cm to 120cm for the Five-year-old, on the patient-detector side resulted in at least 25% cardiac and skin entrance dose rate increase for both age groups. Techniques #7-8: For the Newborn, switching to lower magnifications, from 6″ to 8″ and 10″, resulted in at least 5% and 30% dose rate reductions, respectively; for the Five-year-old, starting at 8″ standard magnification, switching to the other 6″ and 10″ magnifications resulted in no clear changes (due to varying effects at different measurement locations) and ~30% dose rate reductions, respectively. Technique #9: Having open collimation, as compared to the standard collimation applied in Technique #1, which is the common, reasonable collimation used by the clinicians during procedures, yielded no significant dose rate changes for both age groups likely because the measurement locations for cardiac and skin entrance were always in the center of the FOV, virtually unaffected by the FOV marginal changes by collimation.

Applying an incorrect Patient Type, that for a typical Five-year-old, to the Newborn resulted in about a factor-of-two increase in cardiac and skin entrance dose, as compared with imaging with correct Patient Type. The exception is the lateral imaging

technique with arms down (#2b), for which a reduction in dose rate was observed. This is likely due to the added attenuation effect of the arm, which offset the increased irradiation output from the X-ray tube.

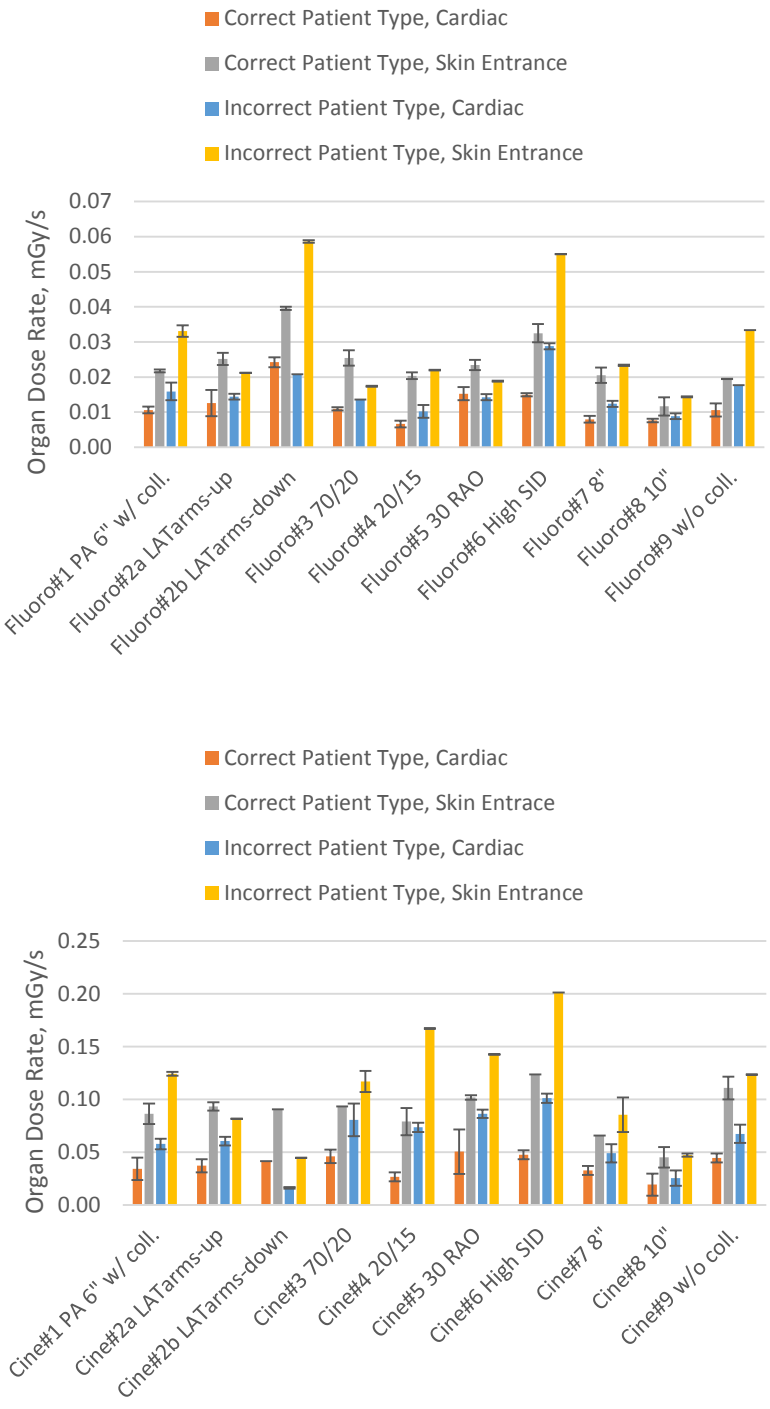

Figure 3.4 Cardiac and skin entrance dose rates, Newborn, correct vs. incorrect Patient Type settings. Top: Fluoro; Bottom: Cine

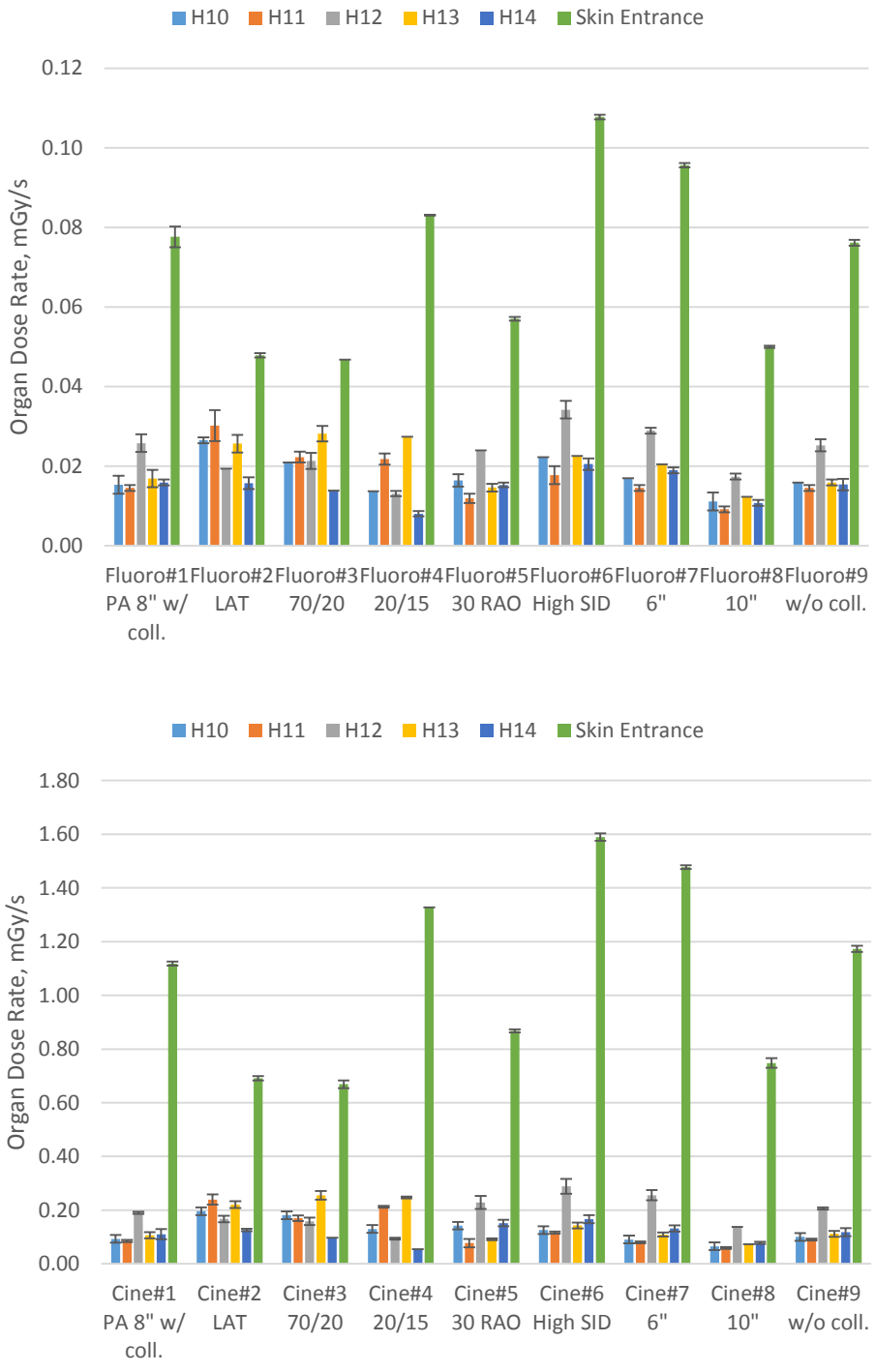

Figure 3.5 Cardiac and skin entrance dose rates, Five-year-old, at various dosimeter locations

The plots of dose index (AK, DAP) rates vs. measured organ (cardiac and skin) dose rates for the Newborn and Five-year-old, for all the Fluoro and Cine imaging techniques, are presented in Figures 3.6 and 3.7 respectively. Linear line-of-best-fit were also displayed, along with the conversion coefficient and R^2 value, for each plot.

Of all dose index vs. organ dose comparisons for both age groups, good linear correlations were only present for AK vs. Cardiac ($R^2 = 0.7213$) and AK vs. Skin Entrance ($R^2 = 0.9355$). Elsewhere, there was lack of any proof that the AK and DAP were good indicators for internal or surface organ dose.

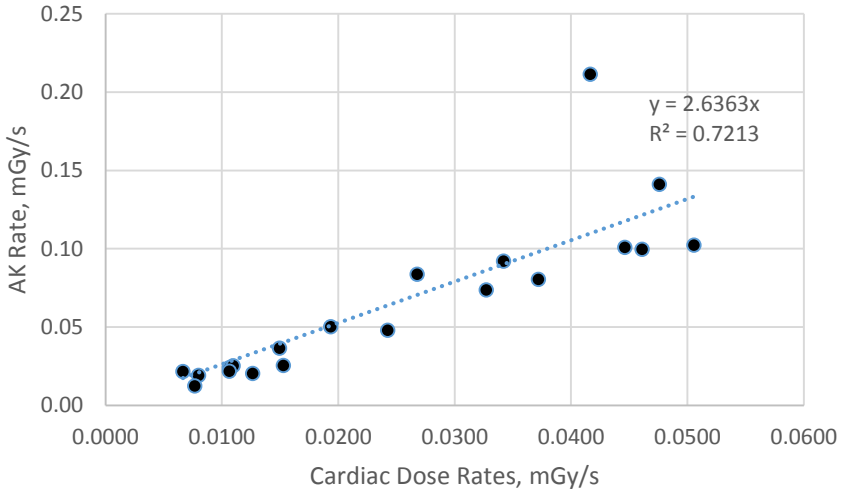

a)

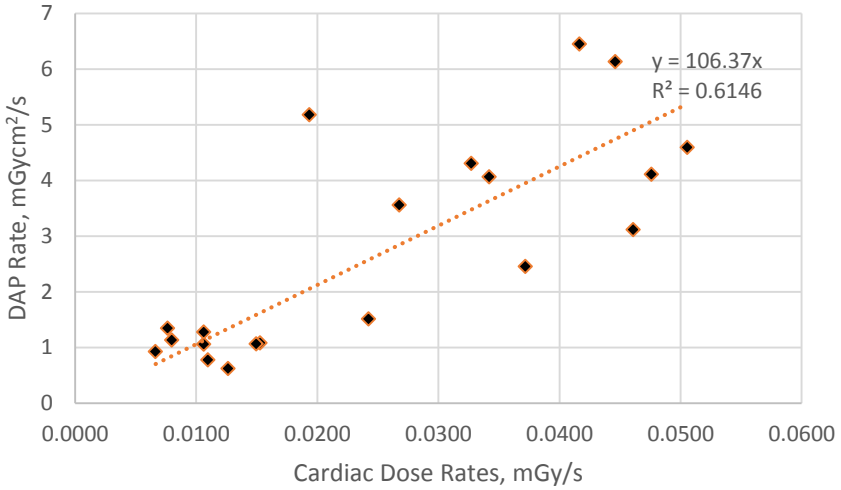
y = 106.37x
R² = 0.6146
DAP Rate, mGycm²/s
Cardiac Dose Rates, mGy/s
0
1
2
3
4
5
6
7
0.0000
0.0100
0.0200
0.0300
0.0400
0.0500
0.0600

b)

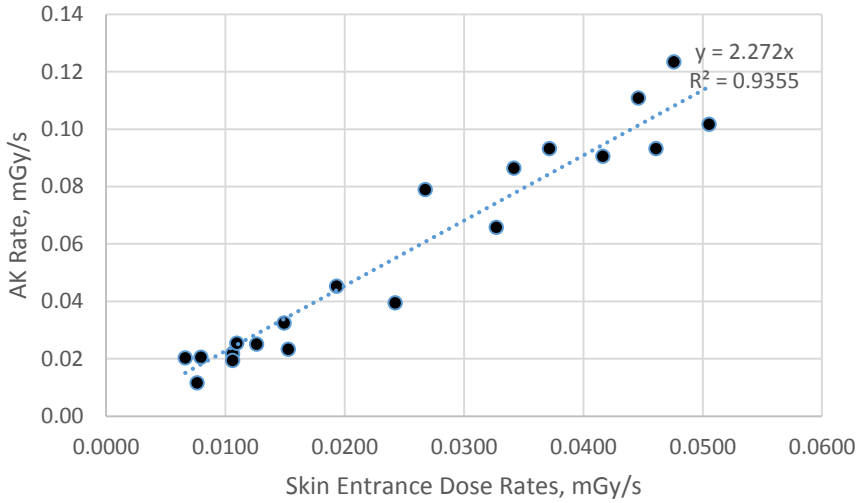
y = 2.272x
R² = 0.9355
AK Rate, mGy/s
Skin Entrance Dose Rates, mGy/s
0.00
0.02
0.04
0.06
0.08
0.10
0.12
0.14
0.0000
0.0100
0.0200
0.0300
0.0400
0.0500
0.0600

c)

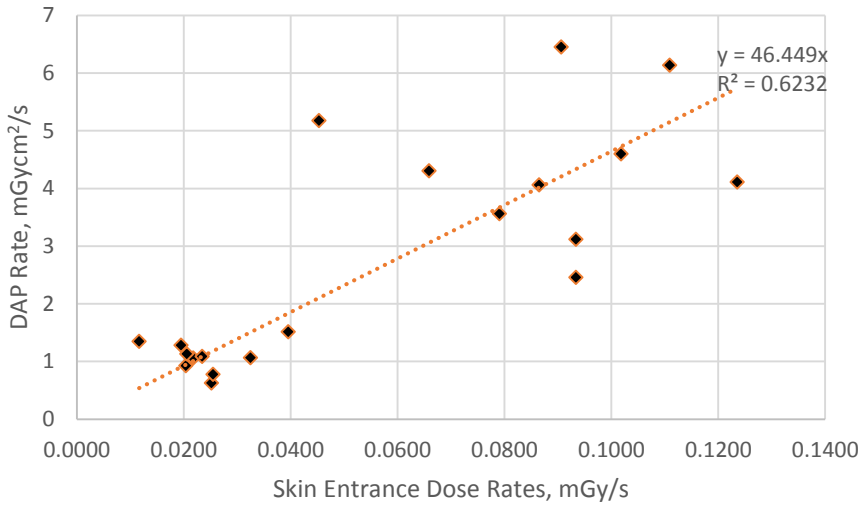

d)

Figure 3.6 Dose index rates vs. measured organ dose rates, Newborn, all nice Fluoro and nine Cine imaging techniques. a) AK vs. Cardiac; b) DAP vs. Cardiac; c) AK vs. Skin Entrance; and d) DAP vs. Skin Entrance

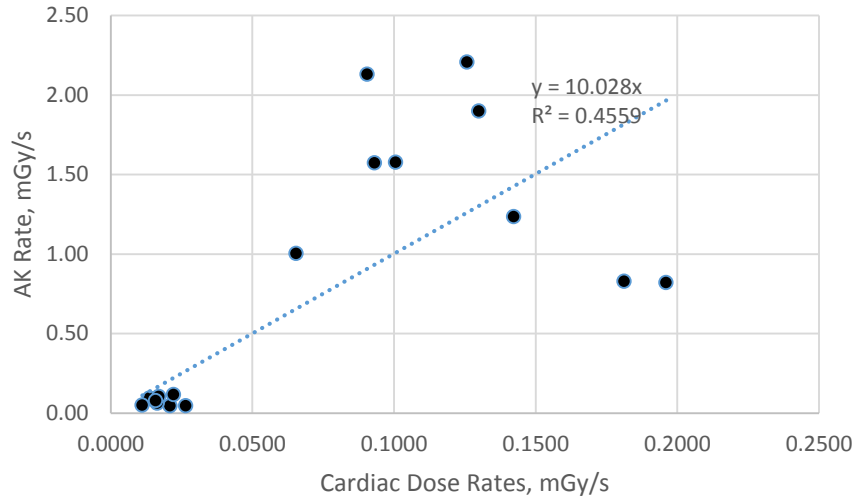
2.50
2.00
1.50
1.00
0.50
0.00
AK Rate, mGy/s
y = 10.028x
R² = 0.4559
0.0000
0.0500
0.1000
0.1500
0.2000
0.2500
Cardiac Dose Rates, mGy/s

a)

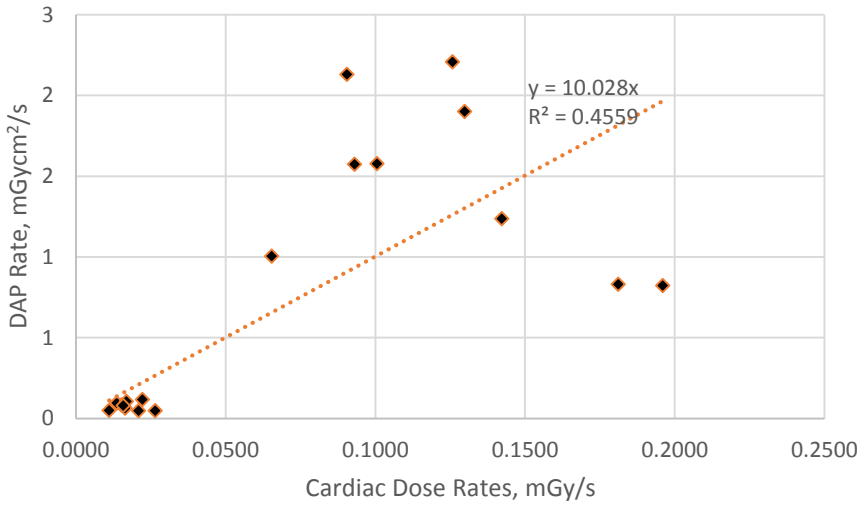
3
2
2
1
1
0
DAP Rate, mGycm²/s
y = 10.028x
R² = 0.4559
0.0000
0.0500
0.1000
0.1500
0.2000
0.2500
Cardiac Dose Rates, mGy/s

b)

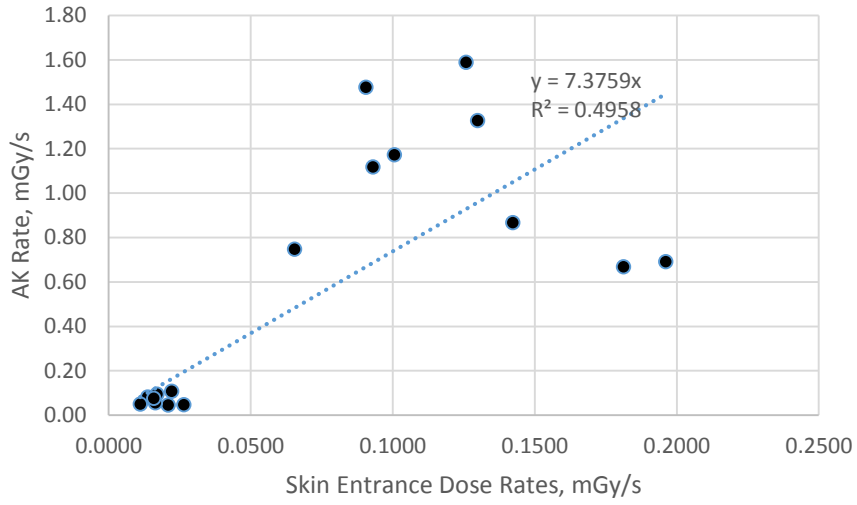

c)

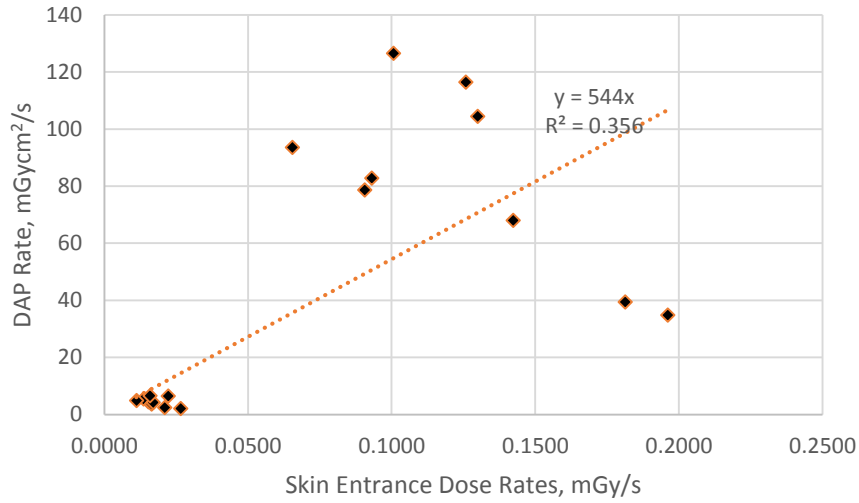

d)

Figure 3.7 Dose index rates vs. measured organ dose rates, Five-year-old, all nine Fluoro and nice Cine imaging techniques. a) AK vs. Cardiac; b) DAP vs. Cardiac; c) AK vs. Skin Entrance; and d) DAP vs. Skin Entrance

3.4 Discussion

By measuring dose rates for one internal (heart) and one surface organ (skin entrance) for two age groups, there are a few of points for discussion from the measured results.

First, the imaging system's own protocol presets are a fundamental factor in patient dose. Examples: 1) The dose rate of Cine is much higher than Fluoro (Figures 3.4 & 3.5), as Cine is designed to provide the best image quality for detailed viewing; and 2) Under correct Patient Type settings, a Five-year-old patient would receive much higher dose rates than a Newborn patient; 3) If a Newborn patient were imaged under the setting for a typical Five-year-old, i.e. Child 35-90 lb – this is important as the console default is at this setting, if not changed – the patient would receive approximately twice the amount of dose as in the situation where the correct settings were applied.

Second, the combinational effects of the automatic tube modulation and variations in patient linear thickness and scattering is another important factor. Examples: 1) Imaging from different projection angles would result in different dose rates even for skin entrance and the heart, even though both organs are at relatively constant distances from the source regardless of the angle; 2) For the Newborn, the positioning of the arms, whether it is "up" by the ears or "down" by the torso, would mean considerably different levels of attenuation in the lateral projection angle, which results in different exposure response, hence different organ dose rates; and 3) For the

Five-year-old, different patterns of dose rates were reported at the five cardiac measurement locations at different projection angles – this brings to the attention of the uneven distribution of cardiac dose due to low-energy X-ray with sensitive dose deposition in a scatter medium of bone, soft tissue, and lung tissue in the patient.

Third, parameters such as the SID and magnification could be difference-makers in imaging optimization. The benefit of collimation has not been determined in the point-dose measurements in this study as both organs measured were in the center of the FOV, virtually unaffected by the collimation changes.

Fourth, the lack of correlation between dose indices and organ doses confirmed our initial concern that the dose indices, when presented as cumulative over a procedure, are insufficient in true patient dosimetry – dose to entire body or to specific organs. There were no universal or consistent dose index-to-organ dose conversion factors based on the Fluoro and Cine imaging techniques studied for the two age groups, so it calls into question about the real dosimetric significance of clinical studies that report only these quantities, with no discrimination of patient age, weight or height. It helped emphasize the importance of organ dose measurements even more for pediatric patients (<18 of age) because of the large variation in size and imaging protocol settings.

To put things into perspective, we can put individual organ dose and AK rates into procedural models to rough-estimate the corresponding cumulative quantities as

well as Fluoro/Cine contributions for "typical" procedures. A recent unpublished internal Duke study at our Pediatric Cardiology division studied 200 cardiac catheterizations in children ≤ 6 years of age and analyzed the imaging usage for each procedure, data shown in Table 3.6. By objective review of the data, the technique usage in the three complexity levels was subjectively defined in Table 3.7.

Table 3.6 Imaging usage of a sample of actual clinical procedures by complexity (Data represent median, 25-75% IQR. Simple interventions included isolated ASD device closure, atrial septostomy, balloon angioplasty of a single pulmonary artery or systemic vein, coil occlusion of a single collateral vessel, PDA device closure, re-coarctation balloon angioplasty, aortic or pulmonary valvuloplasty. Complex interventions were defined as any catheterization involving > 1 intervention or any catheterization involving pulmonary artery or aortic stent placement, coarctation balloon angioplasty or stent placement, aortic valvuloplasty.)

	Diagnostic Cath/Biopsy	Simple Intervention	Complex Intervention
Fluoroscopy time, min	18.6 (10.9 – 25.7)	22.5 (15.0 – 36.4)	34.4 (25.0 – 58.9)
# Biplane Cineangiograms	4.5 (3.0 – 6.3)	6.0 (4.0 – 8.5)	10.5 (7.5 – 13.0)
Cineangiograms length, sec	5.0 (4.1 – 6.3)	5.0 (4.0 – 5.7)	5.2 (3.9 – 6.5)

Table 3.7 Simplified imaging usage in three procedure complexity levels

Complexity	**Technique Usage Composition**
Low	10 min Fluoro time (2/3rds PA and 1/3rd Lateral) + 2 x 4s biplane Cine
Medium	20 min Fluoro time (2/3rds PA and 1/3rd Lateral) + 4 x 5s biplane Cine
High	50 min Fluoro time (2/3rds PA and 1/3rd Lateral) + 8 x 5s biplane Cine

The total estimated cardiac dose, skin entrance dose, AK are shown in Figures 3.8, 3.9 and 3.10, respectively. Based on the estimations, it can be seen that, over an entire

procedure, Fluoro imaging contributes much more dose to the patient than Cine imaging, due to the long fluoro time. In addition, at High complexity, the total skin entrance dose can be around 76 mGy for the Newborn and 276 mGy for the Five-year-old, and the total cardiac dose can be around 37 mGy for the Newborn and 69 mGy for the Five-year-old. Note that this is based on the median values of exposure times of high complexity procedures, greater doses are possible.

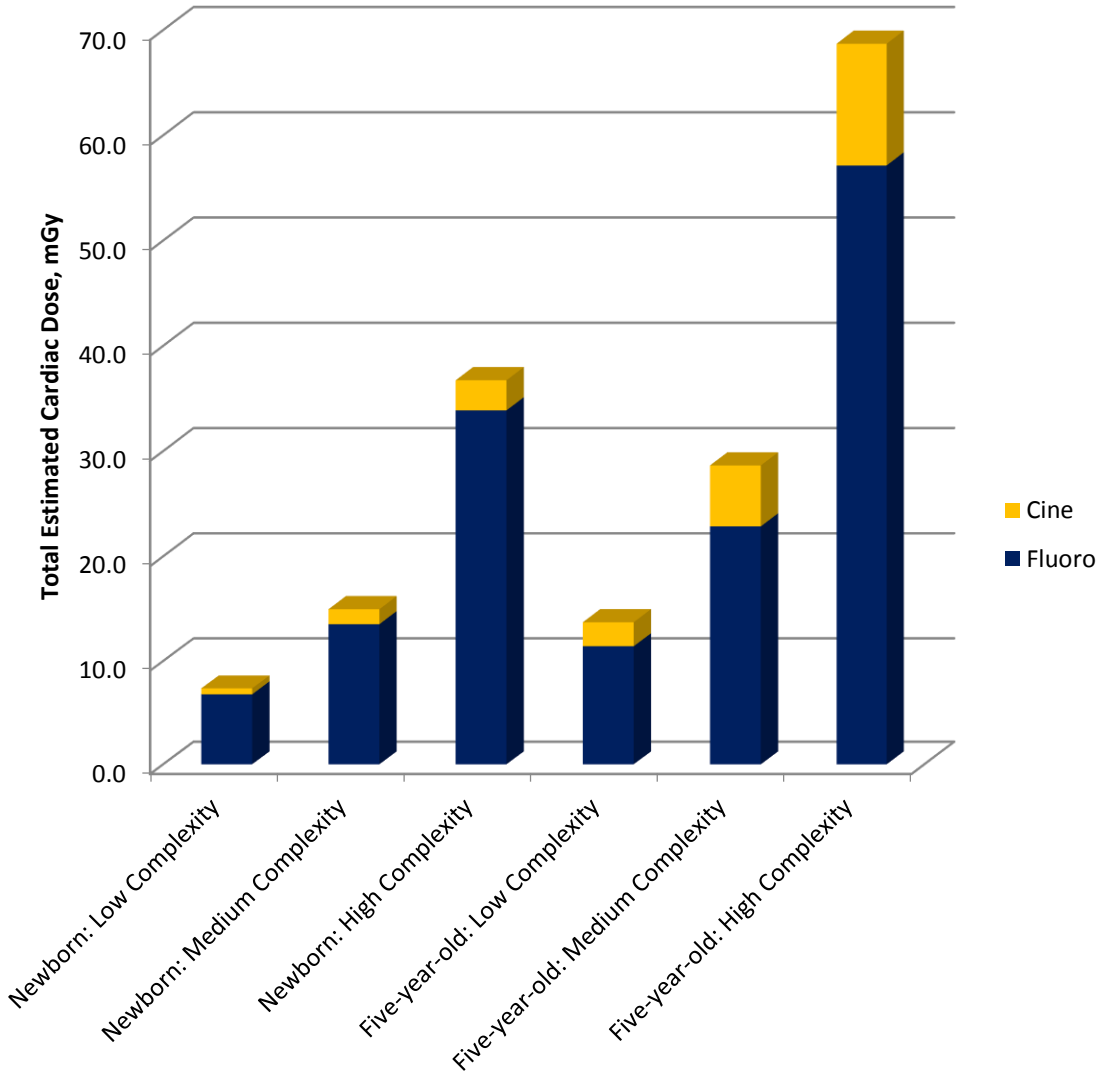

Figure 3.8 Estimated cardiac dose from Fluoroscopy and Cine, based on predefined imaging usages at three complexity levels

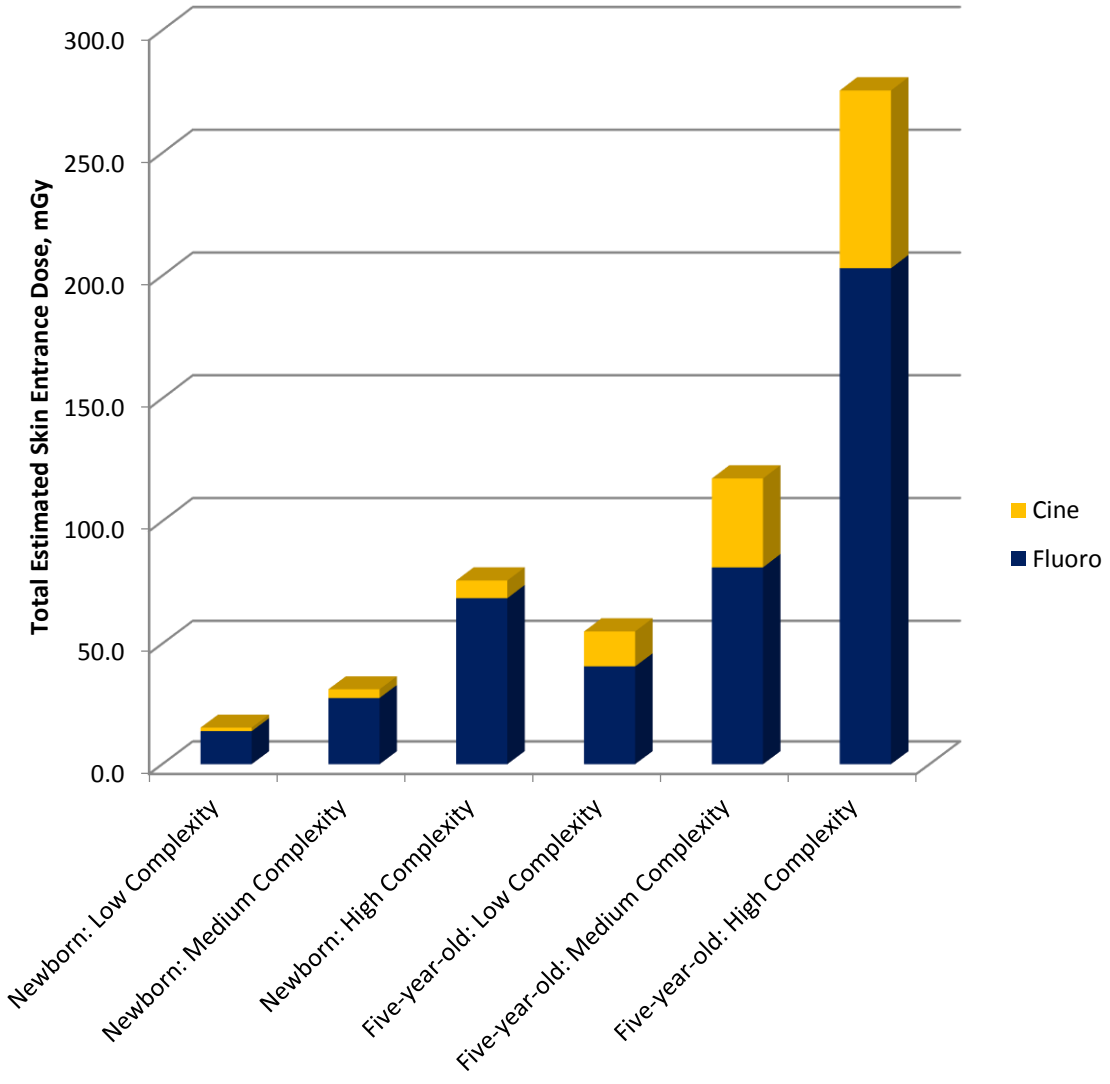

Figure 3.9 Estimated skin entrance dose from Fluoroscopy and Cine, based on predefined imaging usages at three complexity levels

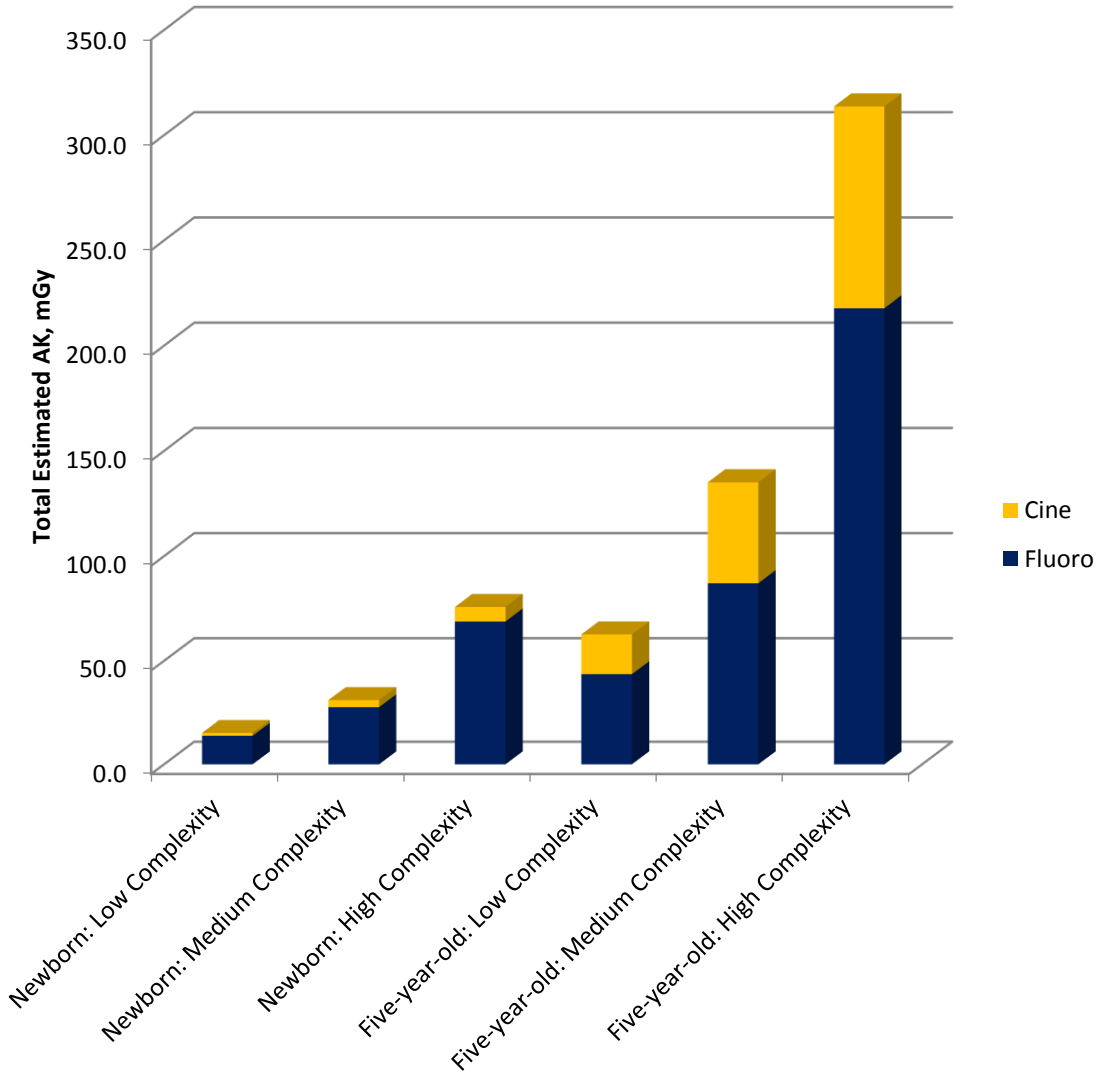

Figure 3.10 Estimated AK from Fluoroscopy and Cine, based on predefined imaging usages at three complexity levels

Though this study is limited to only one imaging system and only two age groups, the general method is simple enough to be applied to other imaging system and other age groups. The limitation is the specificity, but specificity is what is needed to take the cardiac catheterization patient dosimetry forward. From the dosimetric point of

view, interventional procedures are too general, i.e. no fixed imaging protocols and largely dependent on clinician's own practice and system's response to the patient parameters, this makes every imaging system, every clinician, every patient and every procedure unique. Taking the measurement to the levels of individual imaging techniques and organs could truly take dosimetry a step further towards personalized patient dosimetry. The imaging technique-specific AK-to-cardiac dose conversion factors would be used in Chapter 5 for procedure- and patient-specific dose reconstructions.

Overall, the mentality with irradiation usage in the catheterization lab should always be the ALARA (as low as reasonably achievable) principle. It means examining all potential areas for dose reduction, as long as sufficient image quality can be maintained to ensure the success of the procedure. On one hand, technological advancements in the imaging systems themselves, such as new image post-processing algorithms, are constantly the motivation for the manufacturers. On the other hand, for the users of the imaging systems for cardiac catheterization, there are ways of dose reduction (imaging optimization) as well. It is absolutely necessary for clinicians to have a good understanding of the imaging system in order to avoid misuse (e.g. using the wrong Patient Type settings) and always use the optimized imaging parameters. Clinical departments should establish risk management structures [43] as well as establishing

patient dosimetry profiles to keep track of radiation dose from repeated scans or procedures.

3.5 Conclusion

In this chapter, cardiac and organ doses were measured for various representative imaging techniques in cardiac catheterization. The quantitative dosimetric effects of SID and magnification were obtained as well. It was found that dose indices such as AK and DAP, cumulative over a procedure, were not sufficient in indicating patient organ dose, because of lack of correlation with cardiac or skin entrance dose.

In the next Chapter, a similar phantom-MOSFET approach will be applied to a whole-body context, to measure the dose of all relevant organs and evaluate the whole-body effective dose for the two patient age groups. The dosimetric effect of the anti-scatter grid will also be examined.

4. Whole-body organ dose measurement for pediatric patients undergoing cardiac catheterization using anthropomorphic phantoms

4.1 Introduction

Following cardiac and skin entrance dose measurements in the previous chapter, this chapter shifts the attention to a slightly broader picture, whole-body ED.

The ED was first introduced in ICRP 26 as a comprehensive radiation-associated health risk index that accounts for the radiosensitivity (for deterministic and stochastic effects) of individual organs.[44] While it was initially aimed for the radiation protection of radiation workers, it has since gained popularity in the medical community as a major index for patient radiation exposure. One of the main reasons for the adoption for medical patient radiation dosimetry is cross-modality comparison – it is a radiation dose quantity that can be determined for patients of all imaging or treatment modalities that use ionizing radiation. By the latest ICRP definition[45], the effective dose, ED, is calculated by using by the following equation

$$ED = \sum_T w_T H_T \qquad \textbf{(Eqn. 1)}$$

where w_T are the committee-defined dimensionless tissue-specific weighting factors and H_T are the tissue-specific equivalent doses in tissue T.

On the other hand, it should be acknowledged that the effective dose is not a perfect dose index in medical applications due to three main limitations. First, there is no age- and sex-specificity in the tissue weight factors, despite of observed specificities

in various lifetime-attributable risks for multiple cancers.[46] Second, the tissue weighting factors are determined by task groups of the ICRP and have been subject to change in recent years. Third, the effective dose essentially is the summation of risks from all organs and tissues in the body, but it can be argued that for certain purposes, it is better to compare and analyze the risks to individual organs rather than the total-body summation.

Despite these limitations, however, it can still be reasoned that, as it may be years before conclusive and comprehensive dose-to-risk understanding is available, the effective dose is still a good radiation dose index for whole-body dose assessments. Therefore for this study, weighing the advantages and limitations, the patient effective dose will be evaluated for techniques with the two most representative projection angles, PA and Lateral, used in cardiac catheterization.

In addition, this study also assessed the ED of the same imaging techniques without the presence of the anti-scatter grid. The anti-scatter grid is a common accessory installed on the surface of the flat-panel detector to improve image quality by stopping scattered photons from reaching the detector. A side-effect of it is that it also absorbs some primary photons, thus potentially reducing total photon rate reaching the detector enough to trigger a considerable increase in dose rate, due to the automatic exposure control in modern systems. Studies for various X-ray based imaging modalities have reported that for imaging of children, which involves relatively less scatter than adults

due to the smaller body size, the disadvantage of dose rate increase may outweigh the benefit of image quality improvement.[47-54] Therefore in this study, the dosimetric effect of the anti-scatter grid use with our imaging system of interest and patients of the Newborn and Five-year-old age groups was examined.

4.2 Methods

4.2.1 Imaging system

As before, the imaging system used was a Allura Xper FD 10/10, as introduced in Section 3.2.1.

The anti-scatter grid is a 70-line grid with a grid ratio (height of the strip/interspace thickness) of 13. The cover plate is made of carbon fiber sheet of 0.5mm thickness and the interspace material is made of synthetic material. The grid can be easily removed without using any tools, see Figure 4.1.

Figure 4.1 Anti-scatter grid removed from the flat-panel detector apparatus.

4.2.4 Imaging techniques

As stated in the Introduction, the measurements in this study involved only the standard PA and Lateral imaging techniques, i.e. Technique #1 and 2 (#2a only, for the Newborn), under Fluoro and Cine, with and without the anti-scatter grid.

With the anti-scatter grid, the imaging parameters for the imagine techniques were the same as shown in Table 3.4.

Without the anti-scatter grid, the corresponding new imaging parameters are shown in Table 4.1.

Table 4.1 PA and Lateral imaging techniques, without the anti-scatter grid. a) Newborn, Fluoro; b) Newborn, Fluoro; c) Five-year-old, Fluoro; and d) Five-year-old, Cine

a) Newborn, Fluoro, Patient Type: "Baby < 10 lb", Grid OFF								
Technique	**C/G-arm**	**kV**	**mA**	**Projection Angle**	**Frame/s**	**SID (cm)**	**Magnification**	**Collimation**
Fluoro#1 PA 6" w/ coll.	C-arm	65	1.7	0/0 (PA)	15	93	6"	Yes
Fluoro #2a LAT (Arms-up)	G-arm	65	1.8	90LAO/0 (Lateral)	15	112	6"	Yes

b) Newborn, Cine, Patient Type: "Baby < 10 lb", Grid OFF								
Technique	**C/G-arm**	**kV**	**mA**	**Projection Angle**	**Frame/s**	**SID (cm)**	**Magnification**	**Collimation**
Cine#1 PA 6" w/ coll.	C-arm	68	9.9	0/0 (PA)	15	93	6"	Yes
Cine #2a LAT (Arms-up)	G-arm	65	106	90LAO/0 (Lateral)	15	112	6"	Yes

c) Five-year-old, Fluoro, Patient Type: "Child 35 – 90 lb", Grid OFF								
Technique	**C/G-arm**	**kV**	**mA**	**Projection Angle**	**Frame/s**	**SID (cm)**	**Magnification**	**Collimation**
Fluoro#1 PA 6" w/ coll.	C-arm	69	3.1	0/0 (PA)	15	93	6"	Yes
Fluoro #2a LAT (Arms-up)	G-arm	67	2.7	90LAO/0 (Lateral)	15	112	6"	Yes

d) Five-year-old, Cine, Patient Type: "Child 35 – 90 lb", Grid OFF								
Technique	**C/G-arm**	**kV**	**mA**	**Projection Angle**	**Frame/s**	**SID (cm)**	**Magnification**	**Collimation**
Cine#1 PA 6" w/ coll.	C-arm	63	238	0/0 (PA)	15	93	6"	Yes
Cine #2a LAT (Arms-up)	G-arm	62	188	90LAO/0 (Lateral)	15	112	6"	Yes

4.2.2 Anthropomorphic phantoms

The same Newborn and Five-year-old phantoms were used as the study in the previous chapter, see Section 3.2.2.

4.2.3 Dosimeter placement

For the Newborn, 20 high-sensitivity MOSFET dosimeter were placed in all relevant internal organs (See Table 4.2) and two 0.18cc ionization chambers were placed on the entrance and exit sides of the skin surfaces.

Table 4.2: MOSFET dosimeter locations for effective dose measurements with the Newborn phantom

MOSFET	Organ	Phantom Slice #	Hole #
A1	Thyroid	6	11
A2	Thymus	7	32
A3	Oesophagus	7	33
A4	Rib (R)	7	25
A5	Rib (L)	7	22
B1	T-Spine	7	26
B2	Lungs (L)	7	18
B3	Lungs (R)	7	20
B4	Breast (L)	7	29
B5	Breast (R)	7	30
C1	Liver	9	60
C2	Stomach	9	61
C3	Stomach	10	72
C4	Pancreas/Spleen	10	77
C5	Kidney (L)	10	82
D1	Kidney/Adrenals (R)	10	83
D2	Pancreas/Upper Colon	10	78
D3	Liver/Gallbladder	11	92
D4	Small Intestines	11	91
D5	Bladder	12	100

To acquire all necessary data, The Five-year-old phantom was measured twice. First, 18 high-sensitivity MOSFET dosimeter were placed in various internal organs except the lungs (See Table 4.3) and two 0.18cc ionization chambers were placed on the entrance and exit sides of the skin surfaces. Second, 14 high-sensitivity MOSFET dosimeters were evenly placed in the left and right lungs (Table 4.4). As we were limited by the number of dosimeters used for each measurement, the two-round approach was necessary to ensure the dose to the lungs were properly measured to account for partial irradiation.

Table 4.3: MOSFET dosimeter locations for effective dose measurements with the Five-year-old phantom; First Round (without lungs)

MOSFET	Organ	Phantom Slice #	Hole #
A1	Thyroid	8	23
A2	Thymus	11	50
A3	Oesophagus	12	51
A4	Rib (R)	13	61
A5	Rib (L)	13	62
B1	T-Spine	13	75
B4	Breast (L)	12	58
B5	Breast (R)	12	59
C1	Liver	15	89
C2	Stomach	15	99
C3	Adrenals(L)	16	112
C4	Pancreas/Spleen/Stomach	15	100
C5	Kidney (L)	16	116
D1	Kidney/Adrenals (R)	16	117
D2	Pancreas/Upper Colon	17	125
D3	Stomach	16	114
D4	Liver/Gallbladder	18	134
D5	Small Intestines	18	142

Table 4.4: MOSFET dosimeter locations for effective dose measurements with the Five-year-old phantom; Second Round (lungs only)

MOSFET	Organ	Phantom Slice #	Hole #
B2	Lungs (L)	10	28
B3	Lungs (R)	10	29
B4	Lungs (L)	11	47
B5	Lungs (R)	11	48
C1	Lungs (R)	11	49
C2	Lungs (L)	12	52
C3	Lungs (L)	12	54
C4	Lungs (R)	12	56
C5	Lungs (L)	13	68
D1	Lungs (R)	13	70
D2	Lungs (R)	13	74
D3	Lungs (L)	14	77
D4	Lungs (L)	14	79
D5	Lungs (R)	14	84

4.2.4 Partial-irradiation correction and effective dose computation

For organs that are partially-irradiated and therefore received non-uniform irradiation, the detector reading taken in the FOV will be corrected to estimate for the average organ dose. The formula is

$$D_{average}=v\ D_{measured} \qquad \textbf{(Eqn. 3)}$$

where $D_{average}$ is the average organ dose, v is the volumetric correction factor for the partially irradiated organs and $D_{measured}$ is average dosimeter readings for the partially-irradiated organs that need correction.

Dose readings at four organs, the Skin, Red Bone Marrow (RBM), Bone Surface and Lungs, were corrected for this purpose in this study.

For the Skin, the two dosimeter readings, at the entrance and exit, were further corrected to the relative proportional skin surface area in the FOV with respect to the whole body. Estimating according to the "Rule of the Nines"[55] – a standardized method used in quick-estimation of estimation proportional skin surface area – the volumetric correction factors, v, were determined to be 32% and 36% when estimated for the Newborn and Five-year-old, respectively.

For the RBM, the dosimeter readings at the various RBM locations were multiplied by the corresponding age-specific RBM distributions, per ICRP 89 data.[56]

For the Bone Surface, the skeletal dose readings (same ones as for the RBM) were corrected by the total skeletal weight distribution, per ICRP 89 data. As the exact distribution of the bone surface cells is not well-understood, the volumetric correction factor, v, was roughly estimated at 20% for both age groups.

For the Lungs, the average of the two dosimeters was used as the estimated average lung dose for the Newborn and the average of the 14 dosimeters was used for the Five-year-old. As the numbers of dosimeters were sufficient for the organ sizes of the respective age groups, no further volumetric correction was necessary.

Similar partial-irradiation dose corrections were performed by Fujii et al in their pediatric CT dosimetry study.[57] The accuracy of this method for effective dose

evaluation in fluoroscopic imaging has also been validated by two other independent studies.[58 59]

The corrected average organ doses were used to evaluate the effective dose using Eqn. 1. The results were normalized to effective dose rate (mSv/s). The fundamental application of the phantom-MOSFET method in diagnostic imaging was previously validated by Yoshizumi et al.[60]

4.3 Results

The whole-body ED rates, with and without the anti-scatter grid, are presented in Tables 4.5 and 4.6, for the Newborn and Five-year-old, respectively. For each imaging technique examined, removing the grid resulted in considerable ED rate reductions – as great as by a factor of two.

Table 4.5: ED rates for the Newborn, with and without the anti-scatter grid

	With Grid				Without Grid			
	Fluoro		Cine		Fluoro		Cine	
	mSv/s	±	mSv/s	±	mSv/s	±	mSv/s	±
PA	0.0042	0.0007	0.018	0.0030	0.0026	0.0007	0.013	0.002
LAT arms-up	0.0059	0.0006	0.026	0.0009	0.0030	0.0005	0.016	0.003
LAT arms-down	0.0080	0.0006	0.015	0.0016	Did not Measure			

Table 4.6: ED rates for the Five-year-old, with and without the anti-scatter grid

	With Grid				Without Grid			
	Fluoro		Cine		Fluoro		Cine	
	mSv/s	±	mSv/s	±	mSv/s	±	mSv/s	±
PA	0.0040	0.0015	0.032	0.006	0.0021	0.0009	0.013	0.006
LAT	0.0041	0.0011	0.031	0.005	0.0032	0.0011	0.020	0.005

The organ dose rates are presented in Figures 4.2 and 4.3 for the Newborn and Five-year-old, respectively. For both age groups, Thymus, Oesophagus, RBM, Bone Surface, Lungs and Breasts (in Lateral imaging only) are directly irradiated and therefore received the highest radiation dose rates. The skin dose rates presented are the estimated average skin dose rates averaged over the whole-body skin surface area, as introduced in the Methods section. The other organs, including Breasts (in PA imaging) received measurable, but small radiation dose rates from scatter radiation.

The effect of imaging from different projection angles (i.e. PA vs. Lateral) was considerable for organs such as thymus, which was irradiated "behind" the largely-attenuating spinal bones when in the PA but not in the Lateral, thus resulting lower dose rates in the PA.

For the Newborn, the position of the arms were shown to be a deciding factor for organ dose as well. With arms down, the lungs receive additional attenuation from the arm on the beam-entrance side, thus received less dose rates than with arms-up. The scenario of putting the arms down by the side of the patient will be always under two counter-acting forces in dose rates, increased dose rates from increased kV and mA and decreased dose rates for organs such as the lungs from the increased attenuation. In our case, the dosimetric effect of the additional attenuation outweighed that of the increased kV and mA. The Five-year-old was not examined for the arms-up or down as the phantom was not equipped with arms.

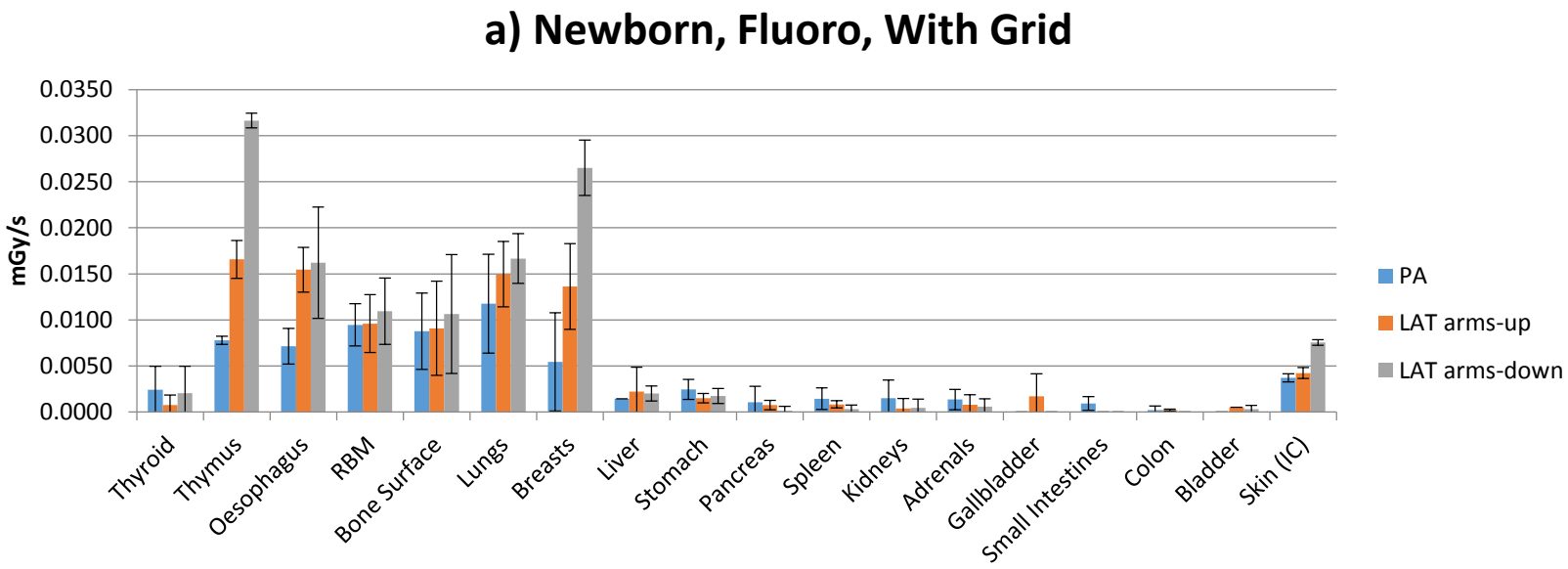
a) Newborn, Fluoro, With Grid
mGy/s
0.0350
0.0300
0.0250
0.0200
0.0150
0.0100
0.0050
0.0000
Thyroid
Thymus
Oesophagus
RBM
Bone Surface
Lungs
Breasts
Liver
Stomach
Pancreas
Spleen
Kidneys
Adrenals
Gallbladder
Small Intestines
Colon
Bladder
Skin (IC)
PA
LAT arms-up
LAT arms-down

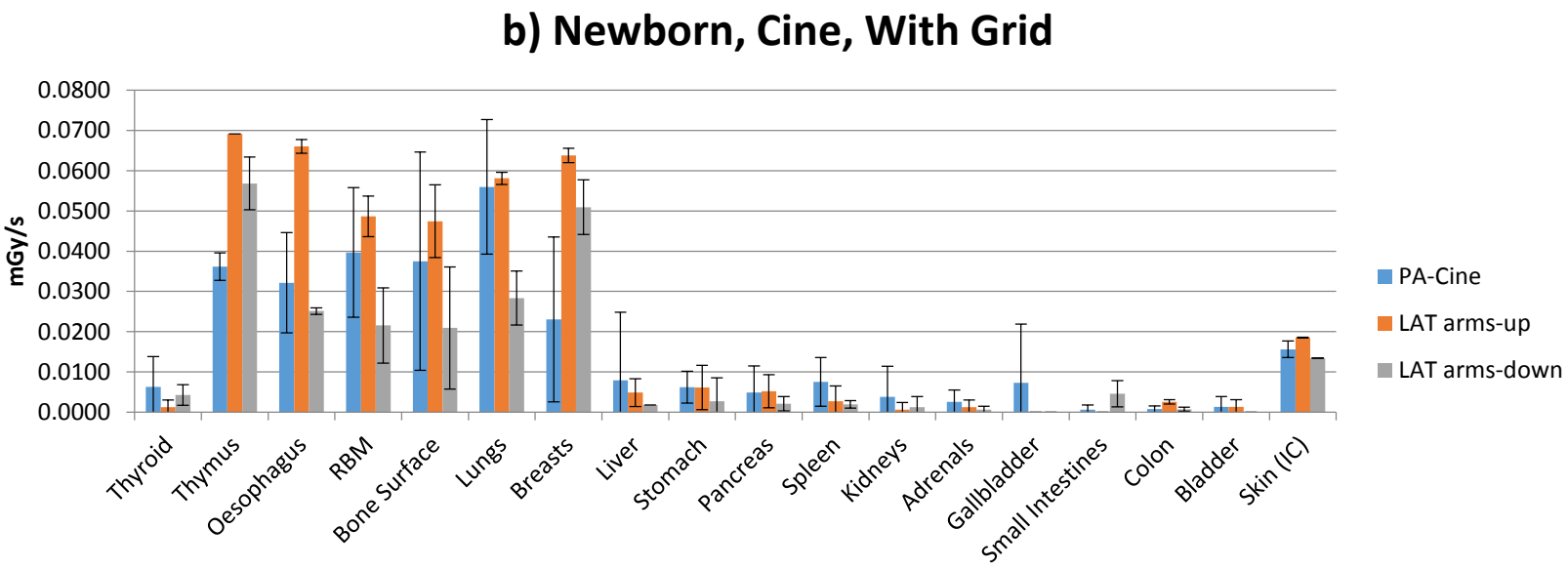
b) Newborn, Cine, With Grid
mGy/s
0.0800
0.0700
0.0600
0.0500
0.0400
0.0300
0.0200
0.0100
0.0000
Thyroid
Thymus
Oesophagus
RBM
Bone Surface
Lungs
Breasts
Liver
Stomach
Pancreas
Spleen
Kidneys
Adrenals
Gallbladder
Small Intestines
Colon
Bladder
Skin (IC)
PA-Cine
LAT arms-up
LAT arms-down

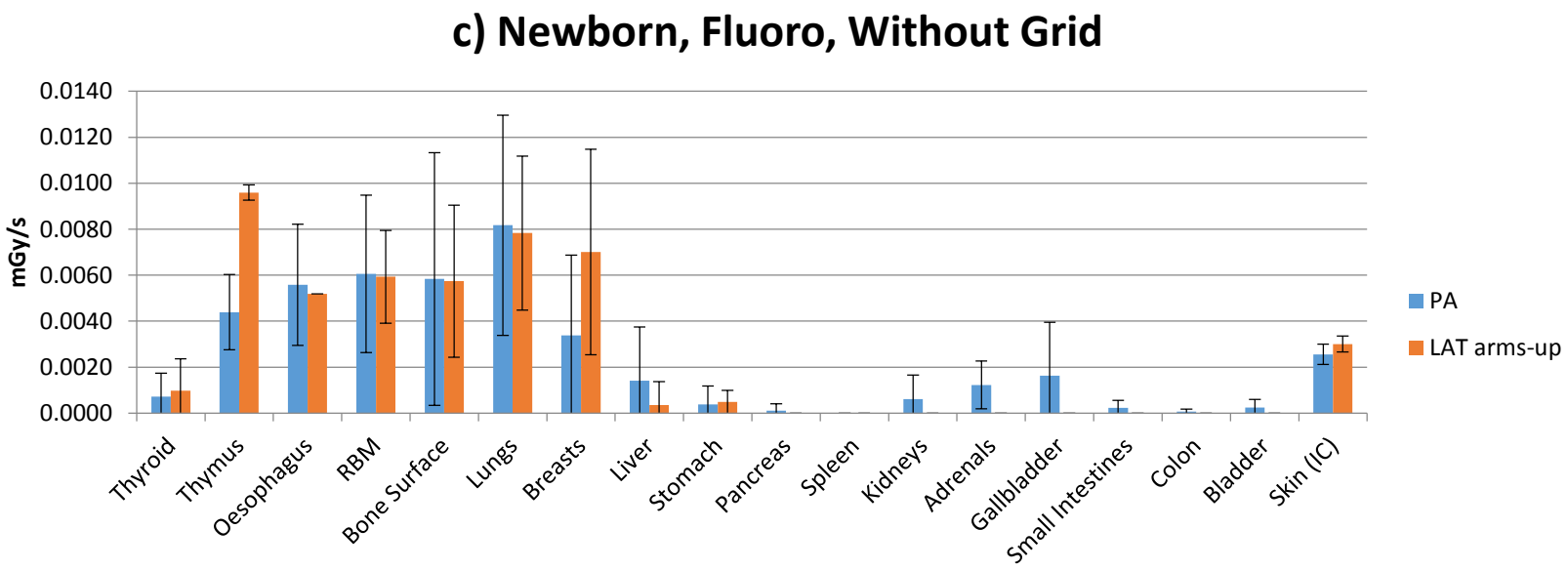
c) Newborn, Fluoro, Without Grid
mGy/s
0.0140
0.0120
0.0100
0.0080
0.0060
0.0040
0.0020
0.0000
Thyroid
Thymus
Oesophagus
RBM
Bone Surface
Lungs
Breasts
Liver
Stomach
Pancreas
Spleen
Kidneys
Adrenals
Gallbladder
Small Intestines
Colon
Bladder
Skin (IC)
PA
LAT arms-up

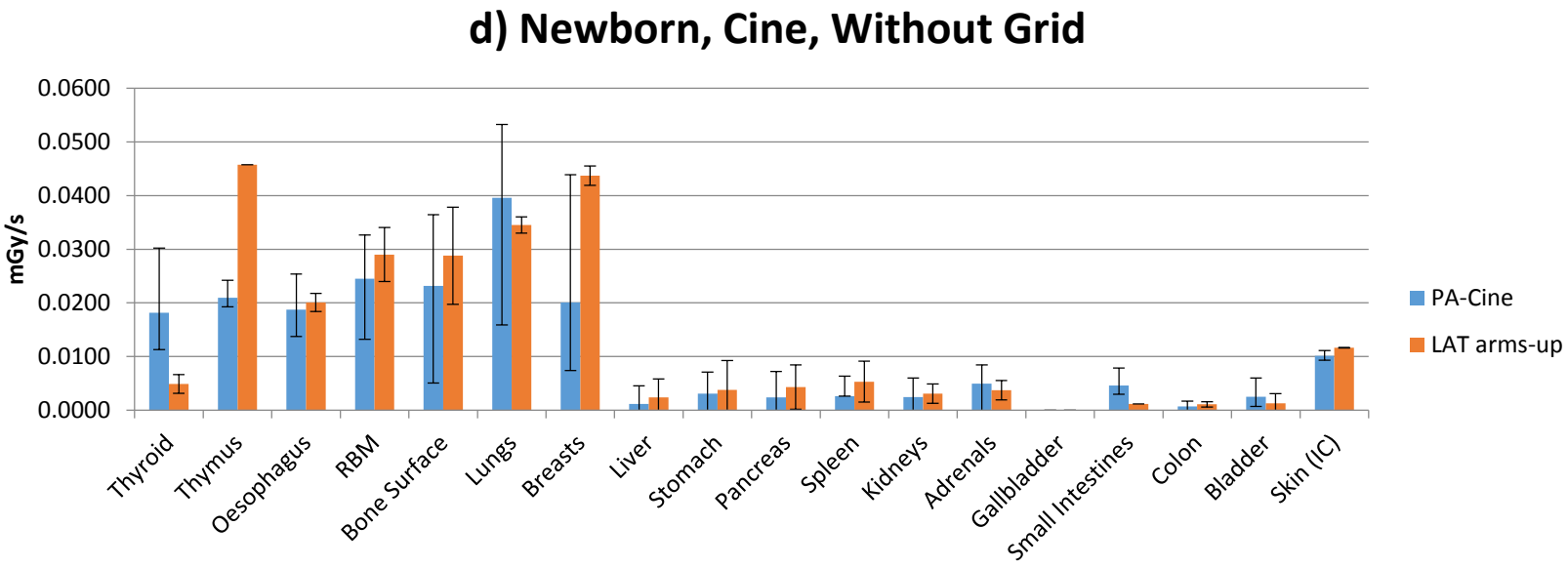

Figure 4.2: Organ dose rates for the Newborn; a) Fluoro, With Grid; b) Cine, With Grid; c) Fluoro, Without Grid; d) Cine, Without Grid.

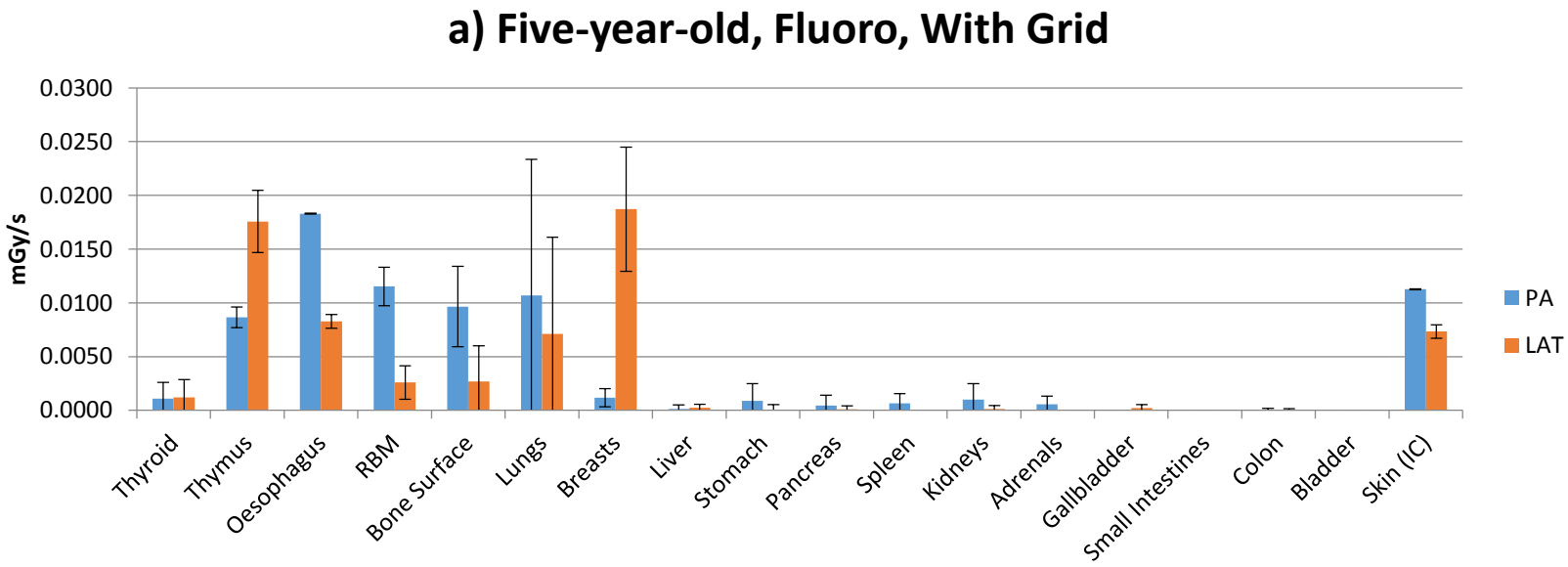
a) Five-year-old, Fluoro, With Grid
mGy/s
0.0300
0.0250
0.0200
0.0150
0.0100
0.0050
0.0000
Thyroid
Thymus
Oesophagus
RBM
Bone Surface
Lungs
Breasts
Liver
Stomach
Pancreas
Spleen
Kidneys
Adrenals
Gallbladder
Small Intestines
Colon
Bladder
Skin (IC)
PA
LAT

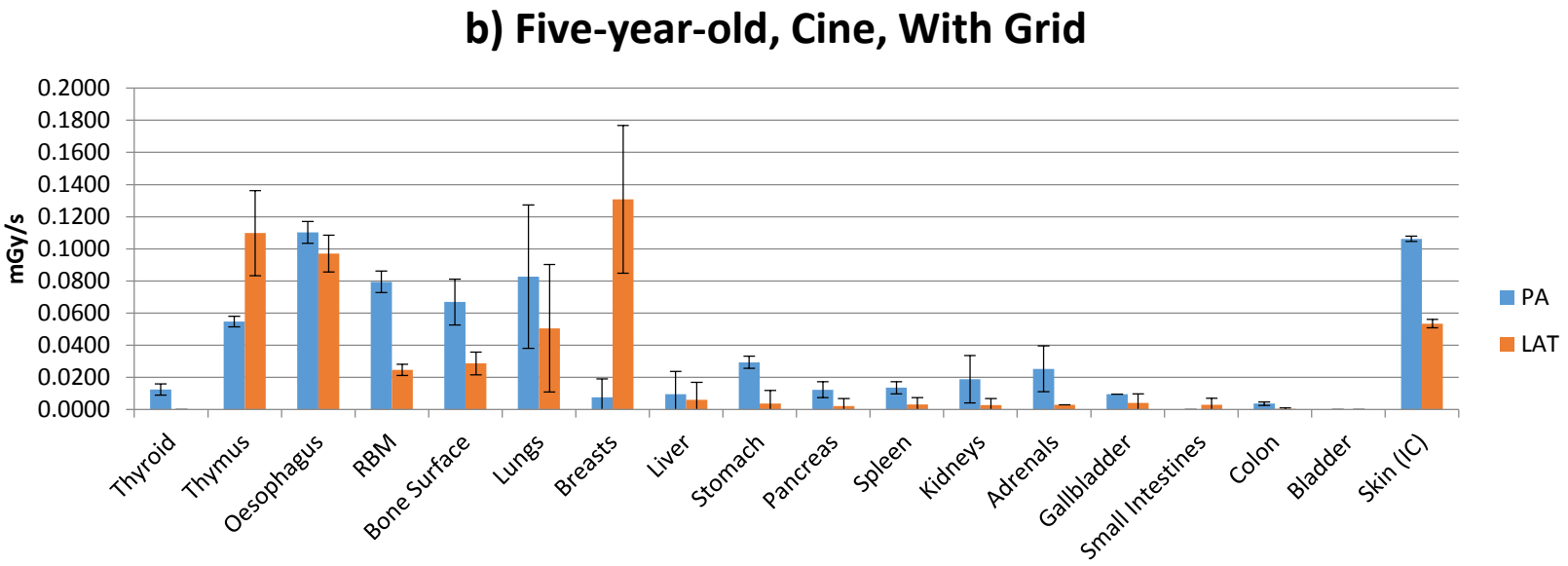
b) Five-year-old, Cine, With Grid
mGy/s
0.2000
0.1800
0.1600
0.1400
0.1200
0.1000
0.0800
0.0600
0.0400
0.0200
0.0000
Thyroid
Thymus
Oesophagus
RBM
Bone Surface
Lungs
Breasts
Liver
Stomach
Pancreas
Spleen
Kidneys
Adrenals
Gallbladder
Small Intestines
Colon
Bladder
Skin (IC)
PA
LAT

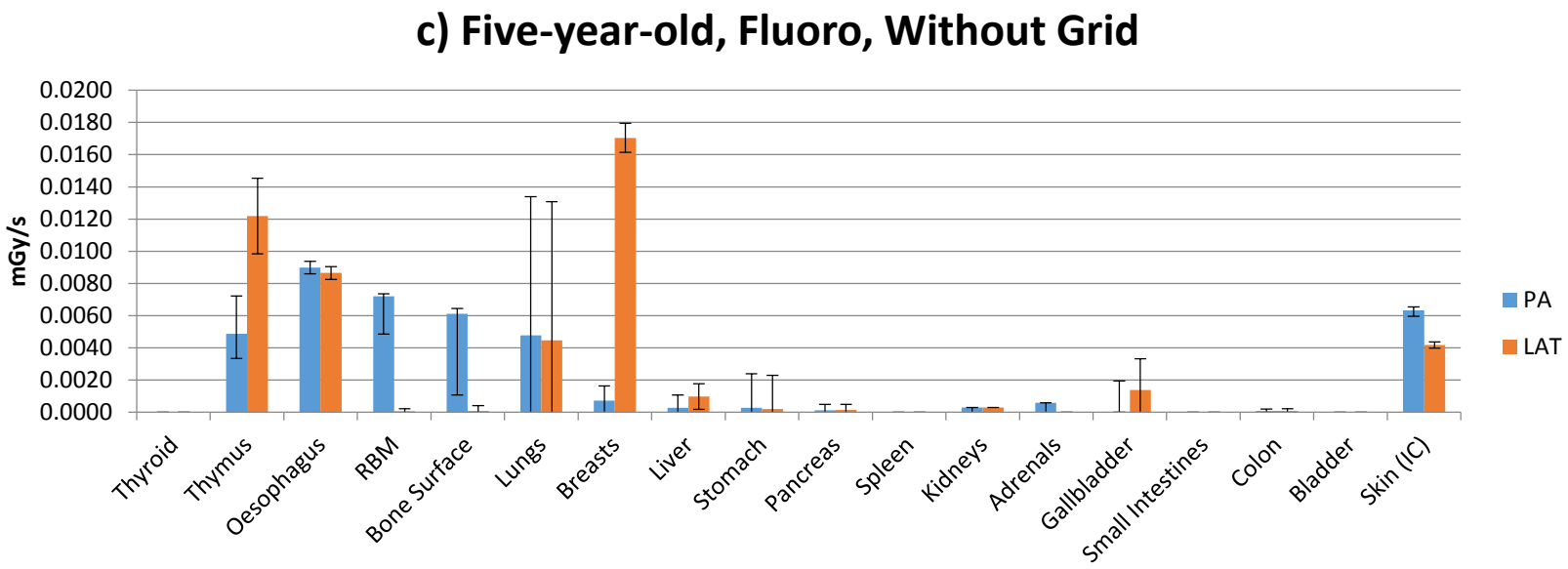
c) Five-year-old, Fluoro, Without Grid
mGy/s
0.0200
0.0180
0.0160
0.0140
0.0120
0.0100
0.0080
0.0060
0.0040
0.0020
0.0000
Thyroid
Thymus
Oesophagus
RBM
Bone Surface
Lungs
Breasts
Liver
Stomach
Pancreas
Spleen
Kidneys
Adrenals
Gallbladder
Small Intestines
Colon
Bladder
Skin (IC)
PA
LAT

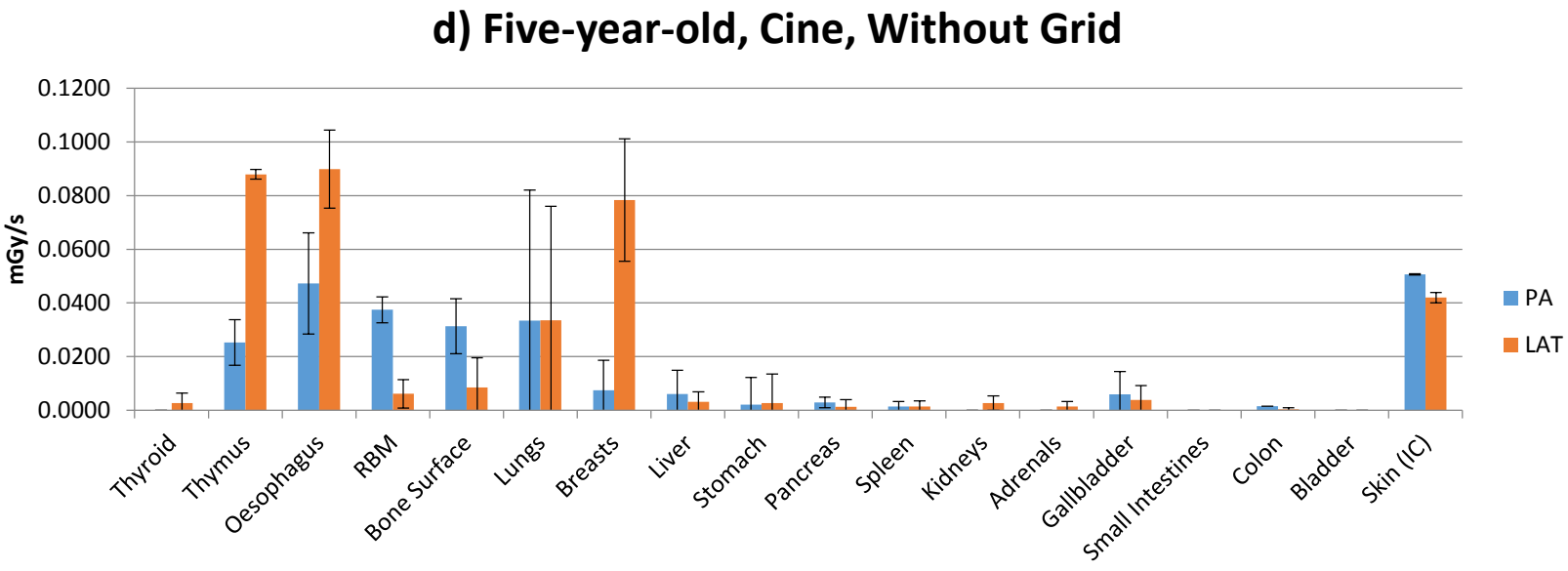

Figure 4.3: Organ dose rates for the Five-year-old; a) Fluoro, With Grid; b) Cine, With Grid; c) Fluoro, Without Grid; d) Cine, Without Grid.

4.4 Discussion

By measuring the dose rates for individual organs and evaluating the whole-body ED rates for PA and Lateral imaging protocols, we acquired a much clearer picture of patient exposure from the fluoroscopic imaging used in cardiac catheterization, compared to only relying on the singular dose indices such as the AK and DAP.

Our results show that imaging without the anti-scatter grid will lead to significant dose rate reductions for the two age groups of patients. This is in agreement with previous studies.[61-68] As the scope of this study is limited to the dosimetric aspect only, the image quality aspect with this study was not considered. Nonetheless, our results in organ dose, physically measured using anthropomorphic phantoms will serve in any future studies that examine the change in image quality with and without the anti-scatter grid.

Assuming the three procedures models used in Table 3.5, the ED for procedures of the three complexity levels were estimated and are presented in Figure 4.4. In Figures 3.8 and 3.9 in the previous chapter, the estimated total cardiac and skin entrance doses were considerably higher for the Five-year-old than for the Newborn; however, as shown in Figure 4.9, the total ED were estimated to be similar for the two age groups. There are two reasons for this. First, the ED accounts for all organs, in and out of the FOV, whereas the skin entrance and heart are both in the FOV. Second, though the Five-

year-old generally was exposed to higher kV and mA's than the Newborn, most of the internal organs of the Five-year-old were irradiated under greater self-shielding, i.e. attenuation from the bigger body size. In addition, similar to Figures 3.8 and 3.9, based on these particular models, the estimated ED were mostly contributed from the Fluoro, rather than Cine.

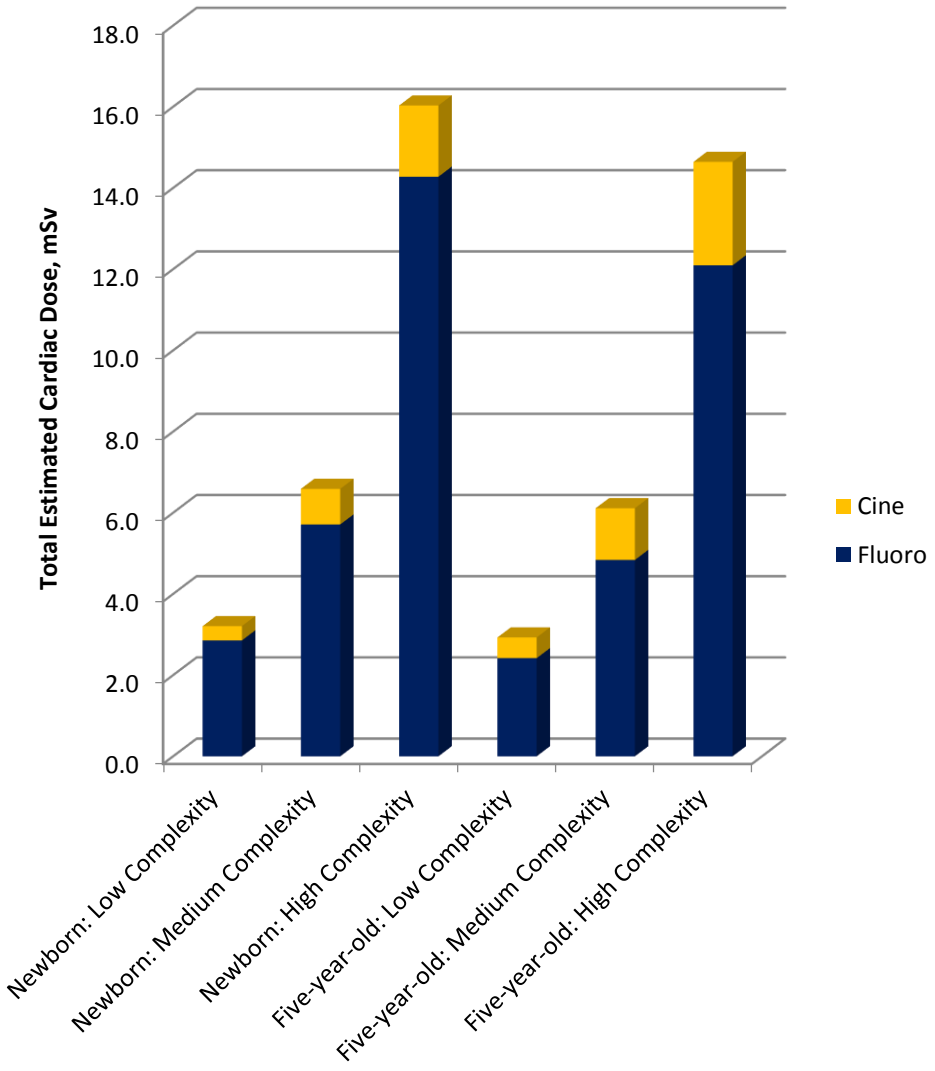

Figure 4.4 Estimated ED from Fluoroscopy and Cine, based on predefined imaging usages at three complexity levels

As discussed earlier, the advantage of ED is its cross-modality comparability. Based on the ED estimations above, a high-complexity cardiac catheterization procedure (~15 mSv) would likely involve much more patient dose than the background radiation in the U.S. (3.0 mSv per year) and a typical chest CT scan (5-7 mSv for adults, may be

much lower for children).[69] And considering repeated procedures and imaging by other modalities, the cumulative patient dose may potentially much higher with great correspondingly greater long-term health risk.

To the best of our knowledge, there are only limited number of studies that evaluated the ED of fluoroscopic imagine protocols used in pediatric cardiac catheterization, mostly due to the limitation in means for organ dose measurement for most clinical research groups. Among the few studies that did, Pantos et al used a dedicated X-ray patient dose estimation software to estimate the procedural total ED based on the cumulative DAP for pediatric patients [70]; and Lai et al used the MOSFET-phantom method – similar to ours – to examine the ED rates of various imaging protocols and various pediatric age groups.[71] The ED rates are in general agreement with similar imaging techniques for these studies, though parallel direct comparison cannot be made due to differences such as parameters settings and site-specific configurations of the systems.

4.5 Conclusion

In the principle of ALARA and the interest of the long-term health of the patient, the study of individual organ doses and the whole-body ED can add great value to the current understanding of pediatric patient radiation dose from cardiac catheterization. The dosimetric benefit of imaging without the anti-scatter grid was quantified and will

help complete future examination of its overall benefit with the inclusion of the aspect of image quality.

Part II: Clinical Component

5. Clinical applications of dosimetry data: Cardiac dose reconstruction & the Optimization Index

5.1 Introduction

In the Chapter 3, we obtained dosimetric information for individual imaging techniques. The ultimate question still remains: How does one estimate the total dose to individual organs, for entire procedures, which could include various combinations of imaging techniques?

Currently, there are three general routes that one can take to attempt to answer this question, but they do not represent realistic solutions because they all have key limitations. First, consider dose indices such as AK and DAP. Our results in Chapter 3 showed that, when used only as cumulative values over an entire procedure, neither of the dose indices, AK and DAP, were sufficient as indicators of patient cardiac or skin dose, at both ages groups. Second, Monte Carlo (MC) simulation-based software, which can be as sophisticated as general-purpose particle-transportation simulation packages such as EGSnrc [72 73] or dedicated clinical dose estimation software such PCXMC (STUK, Helsinki, Finland). The current limitation with taking this route lies in the high variabilities of each procedure, which would require considerable time- and manpower consumption in making the individual setups and validation, which likely requires physical measurements. Third, biodosimetry, particularly the biomarker, γ-H2AX foci, has been shown to have potential[74]. However, for biodosimetric methods, sensitivity and low-limit of detection can be persistent limiting factors in clinical imaging applications;

in addition, the non-whole-body irradiation nature of imaging usage in cardiac catheterization requires further research for accuracy and potential variabilities.

In this Section 5.2 of chapter, we first propose a new general organ dose reconstruction formulation, taking the cardiac dose as a proof-of-principle, by incorporating the following: 1) technique-specific dosimetry data previously collected; 2) imaging usage patterns, estimated by experienced clinicians; and 3) relevant information of the actual procedures for which the dose reconstruction is performed. The proposed formulation would then be validated, using an alternative, fundamental formulation which is basically accounting for dose from individual imaging techniques – it is more accurate but impractical in universal application. The validation involved using a dataset of information from clinical procedures with fitting patient criteria for both the Newborn and Five-year-old age groups.

Further in Section 5.3, a variation of the proposed cardiac dose reconstruction formulation was used to estimate for AK. And by comparing the estimated and the actual cumulative AK of the procedure, we propose a new index, Optimization Index, which indicates the level of optimization in imaging usage for a procedure. The Optimization Index was then applied to the same dataset of clinical procedures with additional fitting patient criteria as a demonstration.

5.2 Cardiac Dose Reconstruction

5.2.1 Formulation

The goal of the dose reconstruction is to estimate the total cardiac dose a patient receives from a cardiac catheterization procedure. As previous results on the Five-year-old have shown that there is uneven dose distribution at different locations of the heart when imaged at different projection angles, for the sake of convenience, we simplify the problem by focusing only on the central location of the heart, which we have measured for both the Newborn and Five-year-old patient age groups. Between the two dose indices, AK is intrinsically the more suitable dose index than DAP with the central cardiac dose, because both the AK and cardiac dose are quantities of point dose.

In Chapter 3, we determined the AK and central cardiac dose rates for both age groups for a range of imaging techniques, from which we derived the age- and technique-specific AK-to-cardiac dose conversion factors (CF):

$$CF_{A,T} = \frac{\dot{D}_{A,T}}{\dot{AK}_{A,T}} \qquad \textbf{(Eqn. 5.1)}$$

where $\dot{D}_{A,T}$ and $\dot{AK}_{A,T}$ are the cardiac dose and AK rates, respectively, for a particular age, A, and imaging technique, T.

Fundamentally, the total cardiac dose from a procedure is the summation of the cardiac doses from all individual imaging techniques, including both Fluoro and Cine techniques, used during the procedure, which can be expressed in the following formula:

$$D_{Total} = \sum_{a,t}^{Fluoro} CF_{a,t}\, AK_{a,t} + \sum_{a,t}^{Cine} CF_{a,t}\, AK_{a,t} \qquad \textbf{(Eqn. 5.2)}$$

where D_{Total} is the total cardiac dose from a procedure, the first summation term represents the total cardiac dose from all Fluoro techniques and the second summation term represents that from all Cine techniques.

Though Eqn. 5.2 is perfectly reasonable, it is impractical because for actual procedures, AK is not reported for each individual technique. In order to construct a practical formulation, we arrived at the following:

$$D_{Total} = tf_{Fluoro}(r_{PA}\dot{D}_{Fluoro,PA} + r_{LAT}\dot{D}_{Fluoro,Lat}) + n\tau f_{Cine}(\dot{D}_{Cine,PA} + \dot{D}_{Cine,LAT}) \qquad \textbf{(Eqn. 5.3)}$$

where the first term on the right-hand side of the equation represents the total dose from Fluoro techniques and the second represents that from Cine techniques; the individual variables are explained in Table 5.1.

Thus, applying the specifications to our study to the general formulation. Eqn. 5.3 becomes

$$D_{Total} = t(\tfrac{2}{3}\dot{D}_{Fluoro,PA} + \tfrac{1}{3}\dot{D}_{Fluoro,Lat}) + n(5\tfrac{sec}{Cine})(2)(\dot{D}_{Cine,PA} + \dot{D}_{Cine,LAT}) \qquad \textbf{(Eqn. 5.4)}$$

Table 5.1 Clarification of the variables in Eqn. 5.4

Variables	Representation, assumptions and conditions	Source of acquisition	Specifications for our study
t	Total Fluoro time	System console	
f_{Fluoro}, f_{Cine}	Frame rate corrections	Phantom measurements compared to actual procedure	f_{Fluoro} = 1; for Fluoro, both the phantom measurement and actual procedures used 15 frames/s. f_{Cine} = 2; for Cine, the phantom measurement used 15 frames/s and actual procedures used 30 frames/s.
r_{PA}, r_{LAT}	Estimated proportions of PA and Lateral, assuming Fluoro imaging involved only PA and Lateral imaging; $r_{PA} + r_{LAT} = 1$	Estimation	$r_{PA} = \frac{2}{3}$; $r_{LAT} = \frac{1}{3}$; Estimated by clinician based on experience and data.
$\dot{D}_{Fluoro,PA}$ $\dot{D}_{Fluoro,Lat}$ $\dot{D}_{Cine,PA}$ $\dot{D}_{Cine,LAT}$	Cardiac dose rates at Fluoro-PA, Fluoro-Lat, Cine-PA and Cine-LAT, respectively.	Measured by phantom studies	See Appendix A. Standard PA and LAT techniques refer to Techniques #1 and 2 (2a arms-up, for Newborn), respectively.
n	Number of Cine runs, assuming biplane (PA + LAT)	System console	
τ	Average duration of a biplane Cine run	Estimation	5 seconds; estimated clinical case data.

5.2.2 Validation

The validity of Eqn. 5.4 was conducted using relevant information from a set of clinical procedures, which was applied to both the Eqns. 5.4 and 5.2.

Through the picture archiving and communication system (PACS) at our institution, the procedure search criteria included cardiac catheterization procedures conducted on the imaging system of interest from 01/01/2014 to 06/30/2015, for patients aged either less than 7 months (Newborn) or between 3 and 7 years (Five-year-old). The search yielded 62 Newborn cases and 53 Five-year-old cases.

Saved DICOM images from Cine runs during these procedures were then accessed through the Xcelera Cardiology Enterprise Viewer (Philips Healthcare, Best, the Netherlands) () to obtain relevant projection angle and AK for Eqns. 5.2. Three assumptions were made in this process: 1) Fluoro imaging was estimated to the same 2/3 PA and 1/3 Lateral proportions as in Eqn. 5.4, due to the complete lack of recording in the system (The system does not save parameters of Fluoro imaging, unless it is a "fluoro save", which is rare comparing to the overall Fluoro usage); 2) Oblique projection angles other than the five involved in the phantom studies were approximated to the nearest studied projection angle (e.g. 35° RAO was treated as 30° RAO); and 3) Small deviations in imaging parameters, between the actual procedures and the standard techniques studied were ignored (e.g. Newborn PA, the procedures used 97cm SID whereas the phantom study used 93cm SID).

The patient cardiac doses, estimated by the proposed formulation and the complex and "built-from-scratch" reconstruction, were plotted against each other in Figures 5.1 and 5.2, for Newborn and Five-year-old, respectively. For both age groups, estimations using the proposed formulation were in consistent agreement (<10% deviation and R^2>85%) with those using the complex formulation. The proposed formulation performs slightly better for the Newborn (R^2 = 0.9739) than the Five-year-old (R^2 = 0.8551), likely because the Newborn patient group had a smaller patient size variation (<7 months) than the Five-year-old patient group did (3-7 years)

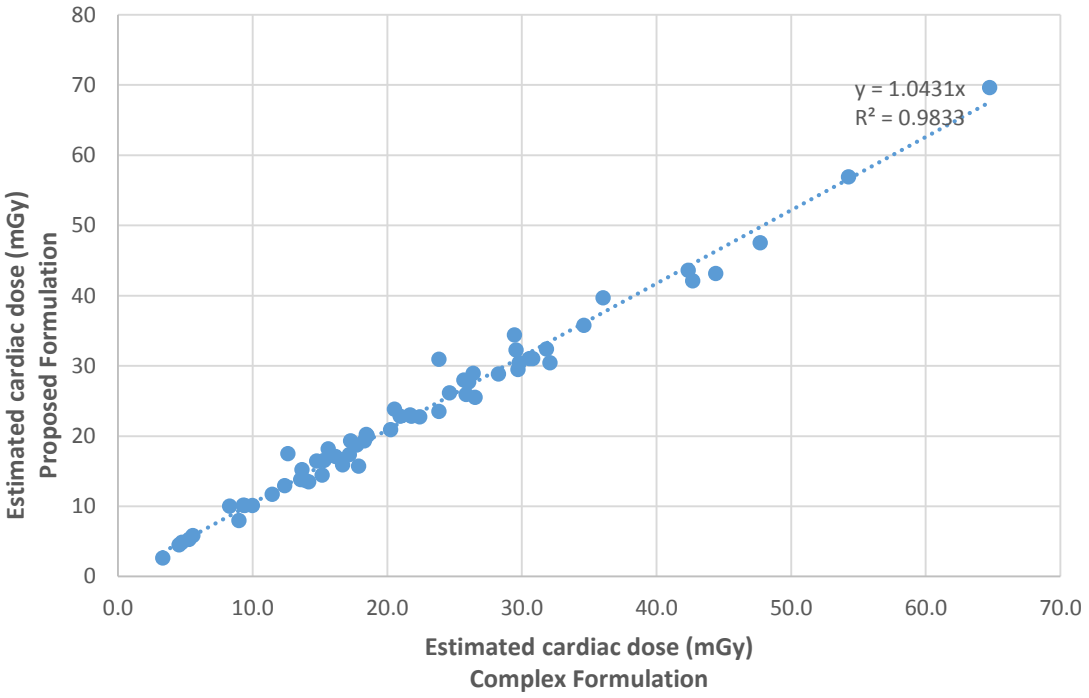

Figure 5.1 Cardiac dose estimated by the proposed formulation vs. the complex formulation, Newborn.

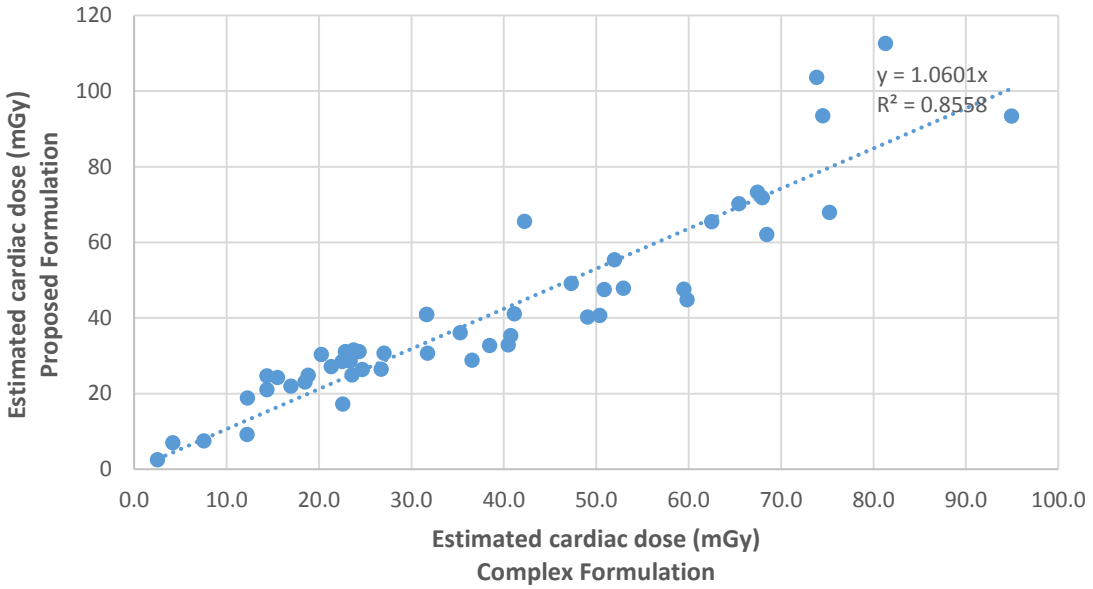

Figure 5.2 Cardiac dose estimated by the proposed formulation vs. the complex formulation, Five-year-old.

5.2.3 Estimated cardiac dose contribution from Fluoro and Cine imaging

As the proposed formulation was validated, it is worthwhile to examine the estimated cardiac dose contributions from Fluoro and Cine imaging for each patient, as presented in Figure 5.3 and 5.4, respectively.

It must be noted that each procedure is unique and independent. Complex procedures would often involve a high level of cardiac dose, contributed from large imaging usage in both Fluoro and Cine.

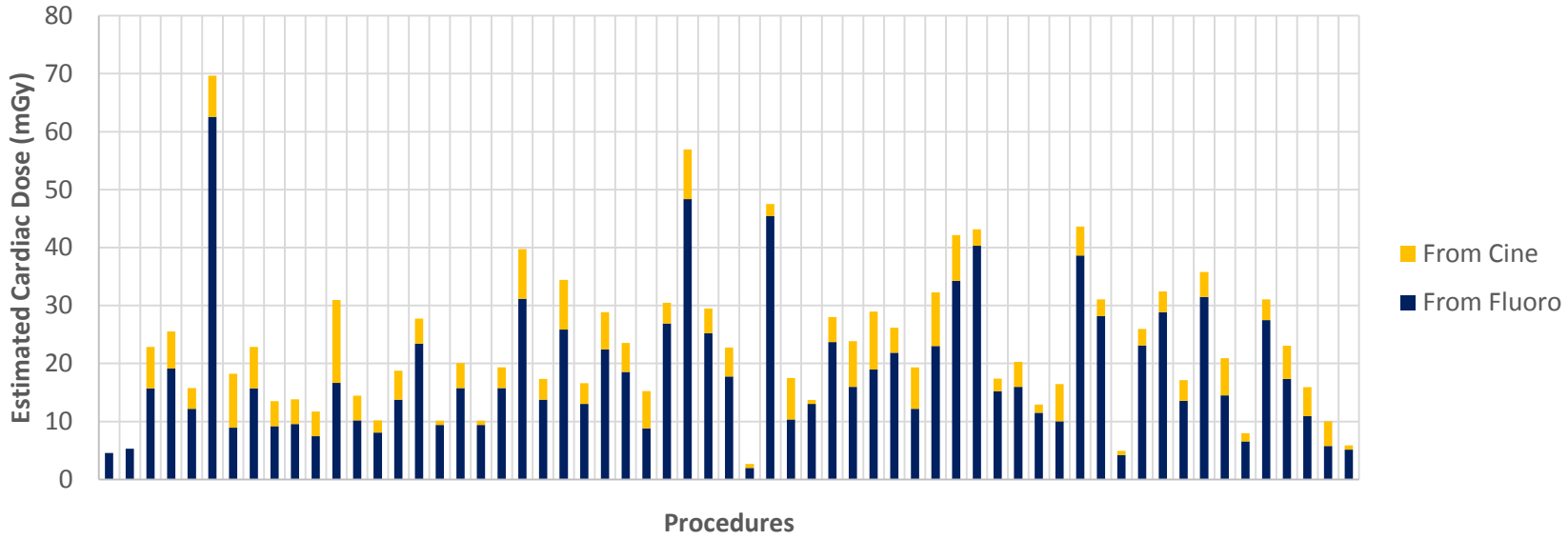

Figure 5.4 Estimated cardiac dose contributions from Fluoro and Cine imaging, Newborn

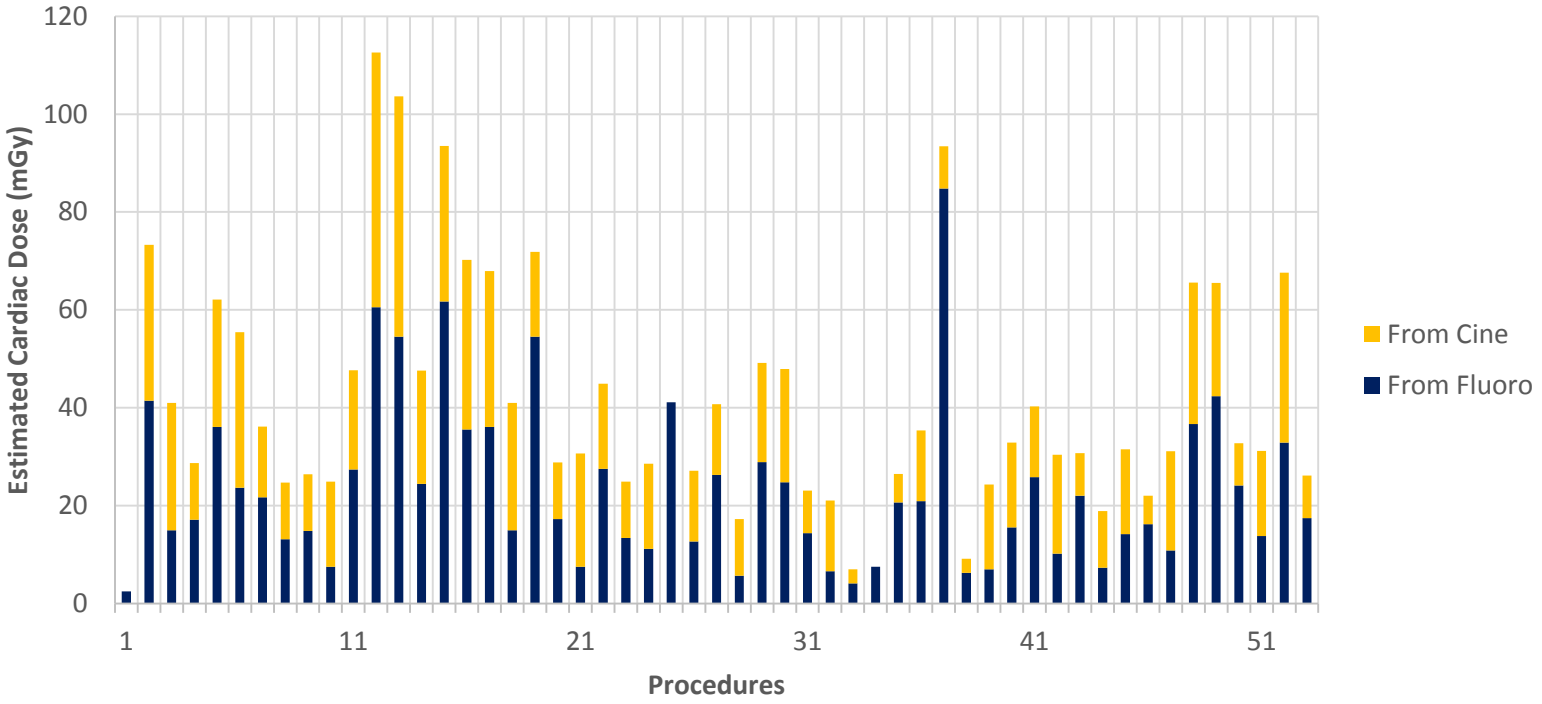

Figure 5.4 Estimated cardiac dose contributions from Fluoro and Cine imaging, Five-year-old

5.3 Optimization Index

5.2.1 Formulation

The patient radiation dose from a cardiac catheterization procedure is largely dependent on a range of factors, such as patient size and procedure complexity. The one factor that is of paramount importance but has never been quantified is imaging optimization. In this section, we propose the new, Optimization Index (OI), to help clinicians to review their imaging optimization during procedures via a quantitative measure and thus to reduce patient dose.

The OI is simply determined as a ratio of two AK's:

$$OI = \frac{AK_{actual}}{AK_{standard}} \qquad \textbf{(Eqn. 5.5)}$$

where AK_{actual} is the actual cumulative AK reported by the system console for a procedure and $AK_{standard}$ is the estimated cumulative AK under the assumption that all imaging was done in a standard construct and level of optimization – it is determined from a variation of the Eqn. 5.4 but instead for AK:

$$AK_{standard} = t(\frac{2}{3}\dot{AK}_{Fluoro,PA} + \frac{1}{3}\dot{AK}_{Fluoro,Lat}) + n(5\frac{sec}{Cine})(2)(\dot{AK}_{Cine,PA} + \dot{AK}_{Cine,LAT})$$

(Eqn. 5.6)

Essentially, the level of imaging optimization was reflected via this simple ratio between the actual AK and the estimated AK if the procedure was conducted in a pre-

defined standard setting. The OI is a unitless quantity that is best expressed as a decimal number. The lower the number, the more optimized the imaging during the procedure.

5.2.3 Application of OI formulation on actual procedures

To demonstrate the application of OI in clinical procedures, the same set of clinical procedures as in Section 5.2 were used, but with stricter selection criteria in patient size for the Five-year-old. Because the OI is a quantity aimed to evaluate the clinician's imaging optimization only and the dosimetric data of the "standard" settings came solely from the phantom measurements, the tested procedures must have body sizes close to that of the phantoms in the two age groups. Thus, qualifying procedures of the Five-year-old (3-7 years of age) were required to have: patient weight of 17 ~ 21 kg (phantom: 19 kg) and height 100 ~ 120 cm (phantom: 110 cm). The Newborn did not require additional criteria as the patient sizes within the age definition (< 7 months) was sufficiently restricted. In total, the qualifying dataset contained 62 Newborn procedures and 15 Five-year-old procedures.

The OI for both ages groups were presented in Figures 5.5 and 5.6. The Newborn procedures had large variations in OI values, four of which are as high as over 5.0 – this is likely because our "standard" patient is at the lower limit in size of the group (i.e. phantom at 0 month of age, selection range is 0-7 months), thus resulting the OI values from the procedures tend to be of greater numerical values. On the other hand, the Five-

year-old procedures reported OI's that are less deviated and lower in numerical value (all 15 procedures had OI of less than 2.0).

The intricacies of the OI will be discussed in the next section.

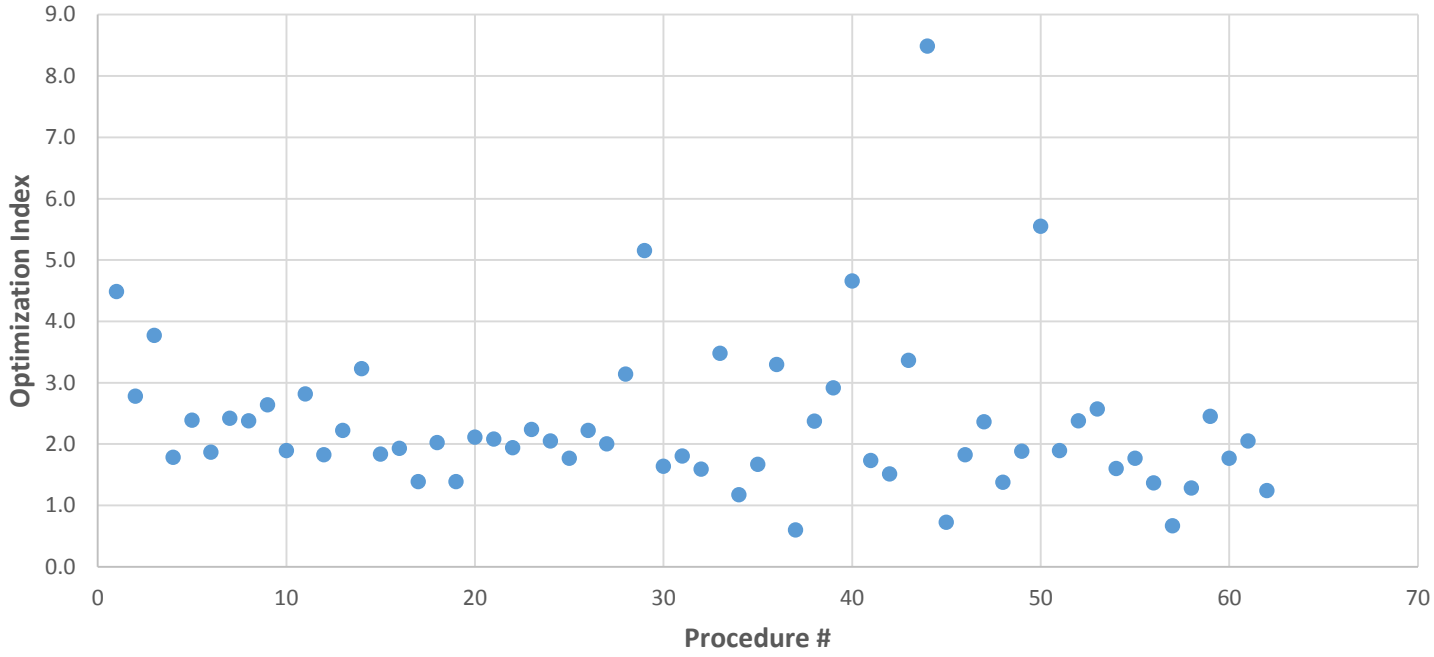

Figure 5.5 Optimization Index on selected procedures, Newborn

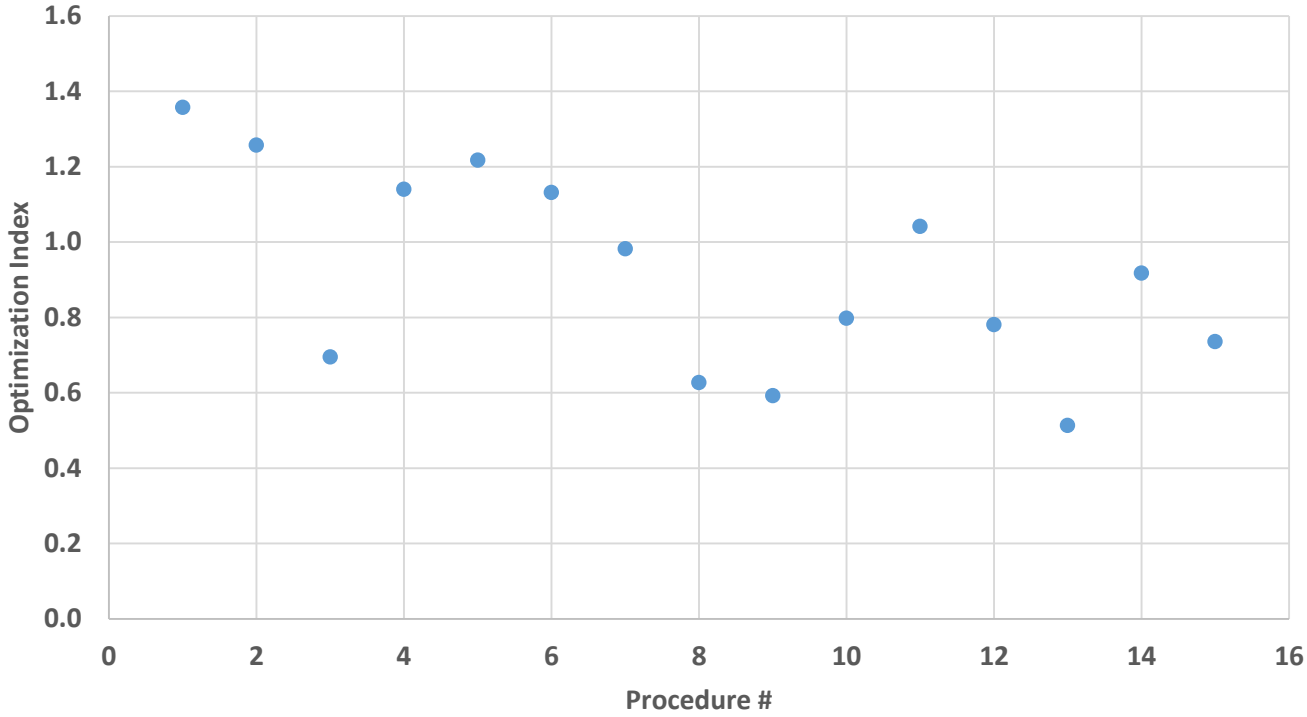

Figure 5.5 Optimization Index on selected procedures, Five-year-old

5.4 Discussion

To the Author's best knowledge, the cardiac dose reconstruction formulation is the first of its kind to bridge the gap between the radiation output and the patient dose received, and the OI is the first of its kind to examine imaging optimization over an entire procedure, instead of at the protocol or technique levels, without involving hardware or software changes.

The applicability is the top advantage of such an algorithmic approach. In applying these formulations, with the availabilities of adequate phantom dose measurements, all one needs to record at the end of a procedure of interest are 1) total AK, 2) total fluoro time, 3) number of Cine runs, and 4) the position of the patients arms (to decide which of the Lateral dose and AK rates to apply).

The proposed OI can be a useful tool in clinician's training because it is intuitive and quantitative. In addition, from the radiation and medical regulator's perspectives, it can also add to a brand new "active" dimension in operator-oriented dose reduction to the existing "passive" paradigm of patient radiation safety management of mostly dose threshold levels.

Admittedly, the current approach is still limited in two main areas. First, the core assumption that the procedures would be conducted in mostly the "standard" way can result in some inaccuracy. Second, the patient groups that the formulations can be applied to are very much limited in age and patient size.

To address the first limitation, one must consider that the purpose of developing such dose reconstruction formulations is to have a common tool that can be easily applied to a large group of patients or cases with an acceptable level of accuracy. Outliers do exist, but one essence of the subject of dose reconstruction in radiation protection is to strike an optimized balance between accuracy and applicability.

The second limitation is perhaps more difficult to address as our approach involves phantom measurements for each patient group as key variables in the formulations. Phantom measurements are the dosimetric basis of our general approach and the most labor-intensive step. With clear targets in clinical research, the general formulations are versatile enough for adaptations for all age groups, imaging systems, institutions and even interventional procedures other than cardiac catheterization.

5.5 Conclusion

In this chapter, we a) developed and validated a cardiac dose reconstruction formulation that can be easily used to retrospectively estimate cardiac dose and b) proposed the Optimization Index that can be used to quantify the imaging optimization, for pediatric patients undergoing cardiac catheterization. The versatility of the formulations allows them to be applied to other age groups, imagine systems, institutions and other types of interventional procedures with fluoroscopic irradiation.

6. Conclusions, Applications and Future Outlook

6.1 Summary and Conclusions

While cardiac catheterization plays a tremendously important role in the diagnostic and therapeutic applications in modern cardiology, one of its main risks is always going to be patient radiation exposure, due to its reliance on fluoroscopic imaging throughout the procedure. As a major patient group of cardiac catheterization, children are subject to potentially greater long-term radiation-associated health risks than adults. Due to the dynamic nature in imaging usage and large variation in patient size and imaging protocol, cardiology has had limited success in the quantitative understanding of radiation dosimetry as well as retrospective radiation dose estimation for pediatric cardiac catheterization.

This dissertation filled this void by walking through the entirety of the problem with custom-developed experiments and analyses. First, we measured the MOSFET dosimeters' angular dependence, with a custom-designed general small-dosimeter angular dependence phantom, to prepare for the dosimetric measurement under the various projection angles in cardiac catheterization. Second, by direct dosimetric measurements with the Newborn and Five-year-old anthropomorphic phantoms on a series of imaging techniques, we obtained a) the baseline technique-specific cardiac and skin entrance dose rates, b) the quantitative dosimetric effects of varying individual parameters, and c) evidence of the insufficiencies of cumulative radiation indices as

indicators for patient dose. Third, we examined the patient radiation exposure in a whole-body perspective which all relevant organ doses as well as the whole-body effective dose were measured and evaluated, respectively, for standard PA and Lateral imaging techniques. Last, we were able to develop a validated retrospective cardiac dose reconstruction formulation and to propose the Optimization Index which evaluates the level of optimization of the clinician's imaging usage during a procedure; and small sample group of actual procedures were used to demonstrate applicability of these formulations.

In its entirety, the research represents a first-of-its-kind comprehensive approach in radiation dosimetry for pediatric cardiac catheterization; and separately, it is also modular enough that each individual section can serve as templates for small-scale dosimetric studies of similar purposes.

6.2 Reproducibility and Notable Sources of Uncertainty

Because cardiac catheterization is a highly dynamic procedure with many moving parts, the patient dosimetry of cardiac catheterization involves a wide range of sources of uncertainty, some of which can be difficult to quantify. Listed below are the most notable ones:

- Statistical dosimeter response variability – quantified by taking the average and standard deviation from multiple measurements.

- Uncertainty from air gap (< 5mm) in phantom holes – Brady[75] measured the response variation between MOSFET (with air gap) and a 0.18cc ionization chamber (without air gap) and in soft-tissue-equivalent material, the same material as the soft tissue portion in the CIRS anthropomorphic phantoms, to be less than 5% deviation.
- MOSFET energy calibration – the dosimeters were calibrated by NIST-traceable 6cc ionization chamber.
- MOSFET angular dependence correction – As described in Chapter 2, the angular dependence correction factors for the five projection angles were at 3% uncertainty.
- AK and DAP accuracy – as explained in Section 1.2, both of these indices are computed from look-up tables whose input parameters are subjected to regularly-scheduled physics quality assurance evaluations to ensure accuracy.
- Phantom positioning – Difficult to quantify but best effort was put forth to ensure the consistency of the positioning
- Patient and phantom size variations – the phantoms only represented the average sizes of their respective groups and certainly the actual patient sizes vary, thus it is virtually impossible to quantify the uncertainty of the phantom-based dose estimation when applied to actual groups of

patients. Therefore, the age- and size-specificities are crucial to the accurate clinical application of the proposed formulations.

- Other variations in actual patient procedures – This item refers to all the other variations in actual procedures from the experimented imaging protocol and techniques, such as projection angle, imaging parameters and FOV. The assumption that all procedures involves the standard imaging techniques as examined in our study was a realistic necessity so that our formulations maintain a balance between accuracy and applicability.

6.3 Areas of Applications and Future Outlook

This dissertation can be useful in the following areas:

1) Personalized patient dose management. Following the rapid advancement in personalized dosimetry for patients of other imaging modalities such as CT, our method can provide the same for pediatric patients of cardiac catheterization – a high-dose item in the long-term recording and tracking of a patient's cumulative medical radiation exposure.

2) Clinician training. Prospectively, clinicians can take advantage of our baseline technique-specific results to quantitatively understand the dosimetric differences between each imaging technique and each variation of individual parameters.

Retrospectively, they have now been provided with the Optimization Index to evaluate the level of optimization in their past procedure in order to improve in the future.

3) Image quality evaluations. No image quality evaluation, for a new imaging protocol or new imaging system, is complete without the dosimetric component.

4) Radiation-associated health effect research. Aside from the relatively better-known skin injuries and cancer, the newly-discovered radiation-associated cardiovascular diseases have already become an active topic in radiobiological research. Pediatric patients undergoing cardiac catheterization are a prime group for epidemiological long-term follow-up studies – with the heart always in the primary organs of imaging and relevant levels of cardiac dose. For a long time the only missing item had been an effective dosimetry method, but it is no longer the case now.

As a proof-of-principle study, this dissertation focused on only two age groups, one imaging system at one institution. As a dynamic procedure with many moving parts and greats ranges in variations – thus potentially significant specificities pertinent to patient dose – it would be obviously beneficial to apply the method on more age groups, more imaging systems and at more institutions. The general dose reconstruction formulation and the Optimization Index can also be adapted for and applied in other interventional procedures involving considerable fluoroscopic imaging, such as chemoembolization for liver cancer treatment.

Further, even in today's highly-competitive, fast-advancing world of medical imaging technology, patient radiation dosimetry research for any imaging modality have a greater role to play than just a part of the "lower dose and better image quality" marketing message of new imaging products. By conducting better and deeper research, personalized radiation dosimetry can realistically improve the paradigm of radiation risk management in medicine in a more forward-thinking direction. For example, our dose reconstruction approach can be integrated into the imaging system as an automatic dose-reporting component. Or, systems could be made more "intelligent" if they are equipped with automatic notifications to clinicians to better their imaging optimization, similar to the idea of the Optimization Index, but reporting before or during a procedure. In addition, as Monte Carlo simulations are likely to become more powerful and effective dosimetric tools in live-imaging scenarios in the foreseeable future, our approach can be adapted to act as an alternative to physically validate the Monte Carlo-oriented dose reporting.

In the end, the ultimate beneficiaries are the patients. This dissertation, radiation dose estimation for pediatric patient undergoing cardiac catheterization, is only a small but significant step forward in the future of medical radiation risk management, which aims for optimized imaging, accident prevention and the fundamental understanding of the radiation-associated health effects.

Appendix A

Numerical data of organ dose and dose index rates in Chapter 3

Table A-1: Organ dose and dose index rates, Newborn, at correct Patient Type setting

	AK Rate	Heart Dose Rate		CF	DAP rate	Skin Entrance Dose Rate	
	mGy/s	mGy/s	±	Heart/AK	mGycm2/s	mGy/s	±
Fluoro#1 PA 6" w/ coll.	0.0242	0.0106	0.0009	0.4384	1.0642	0.0218	0.0004
Fluoro#2a LATarms-up	0.0204	0.0126	0.0038	0.6179	0.6283	0.0251	0.0017
Fluoro#2b LATarms-down	0.0480	0.0242	0.0014	0.5053	1.5208	0.0395	0.0004
Fluoro#3 70/20	0.0254	0.0110	0.0005	0.4323	0.7808	0.0254	0.0022
Fluoro#4 20/15	0.0217	0.0066	0.0009	0.3063	0.9300	0.0204	0.0010
Fluoro#5 30 RAO	0.0255	0.0153	0.0019	0.5991	1.0883	0.0234	0.0014
Fluoro#6 High SID	0.0365	0.0149	0.0005	0.4091	1.0708	0.0325	0.0026
Fluoro#7 8"	0.0192	0.0080	0.0009	0.4142	1.1367	0.0205	0.0022
Fluoro#8 10"	0.0126	0.0076	0.0005	0.6058	1.3508	0.0116	0.0026
Fluoro#9 w/o coll.	0.0219	0.0106	0.0019	0.4856	1.2858	0.0195	0.0000
Cine#1 PA 6" w/ coll.	0.0922	0.0342	0.0105	0.3711	4.0672	0.0865	0.0097
Cine#2a LATarms-up	0.0806	0.0372	0.0063	0.4615	2.4590	0.0933	0.0039
Cine#2b LATarms-down	0.2113	0.0416	0.0000	0.1970	6.4552	0.0906	0.0000
Cine#3 70/20	0.0996	0.0461	0.0063	0.4627	3.1231	0.0933	0.0000
Cine#4 20/15	0.0838	0.0268	0.0042	0.3195	3.5634	0.0790	0.0129
Cine#5 30 RAO	0.1023	0.0506	0.0210	0.4943	4.6007	0.1018	0.0021
Cine#6 High SID	0.1411	0.0476	0.0042	0.3373	4.1157	0.1235	0.0000
Cine#7 8"	0.0738	0.0327	0.0042	0.4430	4.3097	0.0659	0.0000
Cine#8 10"	0.0502	0.0193	0.0105	0.3852	5.1828	0.0453	0.0097
Cine#9 w/o coll.	0.1010	0.0446	0.0042	0.4418	6.1381	0.1109	0.0107

Table A-2: Organ dose and dose index rates, Newborn, at incorrect Patient Type setting

	AK Rate	Heart Dose Rate		CF	DAP rate	Skin Entrance Dose Rate	
	mGy/s	mGy/s	±	Heart/AK	mGycm2/s	mGy/s	±
Fluoro#1 PA 6" w/ coll.	0.0475	0.0159	0.0025	0.3352	1.9167	0.0331	0.0017
Fluoro#2a LATarms-up	0.0245	0.0144	0.0008	0.5887	0.8033	0.0212	0.0000
Fluoro#2b LATarms-down	0.0636	0.0208	0.0000	0.3265	2.1200	0.0586	0.0004
Fluoro#3 70/20	0.0403	0.0136	0.0000	0.3380	1.3117	0.0174	0.0001
Fluoro#4 20/15	0.0345	0.0102	0.0018	0.2965	1.4183	0.0220	0.0001
Fluoro#5 30 RAO	0.0308	0.0143	0.0009	0.4626	1.2567	0.0188	0.0001
Fluoro#6 High SID	0.0792	0.0288	0.0009	0.3636	3.1817	0.0550	0.0001
Fluoro#7 8"	0.0328	0.0124	0.0008	0.3780	1.8967	0.0234	0.0002
Fluoro#8 10"	0.0191	0.0088	0.0008	0.4638	1.8117	0.0144	0.0001
Fluoro#9 w/o coll.	0.0448	0.0177	0.0000	0.3952	3.2050	0.0334	0.0000
Cine#1 PA 6" w/ coll.	0.1806	0.0578	0.0050	0.3200	7.5530	0.1242	0.0019
Cine#2a LATarms-up	0.0938	0.0605	0.0041	0.6452	3.1417	0.0818	0.0001
Cine#2b LATarms-down	0.0496	0.0162	0.0008	0.3263	1.6333	0.0447	0.0001
Cine#3 70/20	0.3517	0.0807	0.0154	0.2295	10.2806	0.1170	0.0099
Cine#4 20/15	0.3218	0.0735	0.0045	0.2284	11.9667	0.1672	0.0005
Cine#5 30 RAO	0.2839	0.0863	0.0039	0.3040	10.6000	0.1426	0.0001
Cine#6 High SID	0.3014	0.1011	0.0043	0.3356	8.9583	0.2013	0.0001
Cine#7 8"	0.1181	0.0490	0.0087	0.4153	7.0750	0.0855	0.0162
Cine#8 10"	0.0633	0.0255	0.0072	0.4033	6.2444	0.0473	0.0016
Cine#9 w/o coll.	0.1672	0.0674	0.0087	0.4034	12.1333	0.1235	0.0001

Table A-3: Organ dose and dose index rates, Five-year-old, at correct Patient Type setting

Imaging Technique	AK rate (mGy/s)	H10 (mGy/s)	± mGy/s	H11 (mGy/s)	± mGy/s	H12 (mGy/s)	± mGy/s	H13 (mGy/s)	± mGy/s	H14 (mGy/s)	± mGy/s	CF H10/AK	DAP rate mGycm2/s	Skin Entrance Dose Rate mGy/s	±
Fluoro#1 PA 8" w/ coll.	0.0848	0.0153	0.0022	0.0145	0.0008	0.0258	0.0022	0.0169	0.0022	0.0159	0.0007	0.1808	4.4983	0.0776	0.0026
Fluoro#2 LAT	0.0482	0.0265	0.0008	0.0302	0.0039	0.0193	0.0000	0.0257	0.0022	0.0157	0.0015	0.5497	2.1233	0.0478	0.0006
Fluoro#3 70/20	0.0480	0.0209	0.0000	0.0222	0.0014	0.0213	0.0020	0.0281	0.0020	0.0138	0.0000	0.4364	2.3933	0.0467	0.0000
Fluoro#4 20/15	0.0959	0.0136	0.0000	0.0218	0.0014	0.0131	0.0007	0.0274	0.0000	0.0080	0.0007	0.1423	5.4217	0.0831	0.0000
Fluoro#5 30 RAO	0.0644	0.0164	0.0015	0.0119	0.0012	0.0240	0.0000	0.0146	0.0010	0.0153	0.0006	0.2550	3.6233	0.0570	0.0005
Fluoro#6 High SID	0.1192	0.0222	0.0000	0.0177	0.0023	0.0342	0.0022	0.0225	0.0000	0.0205	0.0014	0.1863	6.5033	0.1077	0.0006
Fluoro#7 6"	0.1073	0.0169	0.0000	0.0145	0.0008	0.0289	0.0007	0.0205	0.0000	0.0190	0.0007	0.1576	4.2150	0.0956	0.0005
Fluoro#8 10"	0.0513	0.0111	0.0022	0.0091	0.0008	0.0173	0.0007	0.0123	0.0000	0.0108	0.0007	0.2165	4.9367	0.0500	0.0003
Fluoro#9 w/o coll.	0.0808	0.0159	0.0000	0.0145	0.0008	0.0252	0.0015	0.0159	0.0007	0.0154	0.0014	0.1962	6.6167	0.0761	0.0007
Cine#1 PA 8" w/ coll.	1.5744	0.0931	0.0036	0.0853	0.0037	0.1898	0.0039	0.1065	0.0110	0.1102	0.0190	0.0591	82.7667	1.1183	0.0074
Cine#2 LAT	0.8230	0.1961	0.0094	0.2394	0.0190	0.1673	0.0121	0.2207	0.0125	0.1258	0.0045	0.2382	34.8207	0.6916	0.0080
Cine#3 70/20	0.8308	0.1812	0.0064	0.1700	0.0099	0.1585	0.0140	0.2551	0.0165	0.0969	0.0000	0.2181	39.4750	0.6688	0.0145
Cine#4 20/15	1.9014	0.1299	0.0066	0.2122	0.0034	0.0938	0.0036	0.2468	0.0034	0.0545	0.0000	0.0683	104.3917	1.3278	0.0000
Cine#5 30 RAO	1.2371	0.1422	0.0118	0.0774	0.0156	0.2287	0.0240	0.0914	0.0035	0.1520	0.0126	0.1150	67.9500	0.8677	0.0058
Cine#6 High SID	2.2083	0.1258	0.0071	0.1164	0.0037	0.2888	0.0272	0.1429	0.0110	0.1667	0.0152	0.0570	116.4333	1.5893	0.0138
Cine#7 6"	2.1312	0.0905	0.0071	0.0802	0.0037	0.2558	0.0194	0.1091	0.0073	0.1317	0.0114	0.0425	78.6417	1.4777	0.0064
Cine#8 10"	1.0053	0.0654	0.0071	0.0595	0.0037	0.1375	0.0000	0.0728	0.0000	0.0780	0.0038	0.0651	93.5250	0.7479	0.0179
Cine#9 w/o coll.	1.5786	0.1006	0.0000	0.0905	0.0037	0.2063	0.0039	0.1117	0.0110	0.1183	0.0152	0.0637	126.4667	1.1732	0.0114

References

1. Park, Myung K. Park's Pediatric Cardiology for Practitioners, 6th Edition. Maryland Heights: Mosby. 2014. Clinical Key. September 21, 2014 Accessed through http://www.clinicalkey.com

2. Gislason A, Hoornaerta B, Davies AG, Cowen AR. Allura Xper Cardiac System Implementation of Automatic Dose Rate Control. 2011. Koninklijke Philips Electronics N.V.

3. U.S. Food and Drug Administration (FDA). 21 C.F.R § 1020.32. Performance Standards for Ionizing Radiation Emitting Products – Fluoroscopic Equipment. Revised as of April 1, 2015.

4. International Electrotechnical Commission. IEC report 60601. Medical electrical equipment—part 2-43: particular requirements for the safety of X-ray equipment for interventional procedures.Geneva: International Electrotechnical Commission; 2000.

5. ICRP, 2007. The 2007 Recommendations of the International Commission on Radiological Protection. ICRP Publication 103. Ann. ICRP 37 (2-4).

6. ICRP, 2012 ICRP Statement on Tissue Reactions / Early and Late Effects of Radiation in Normal Tissues and Organs – Threshold Doses for Tissue Reactions in a Radiation Protection Context. ICRP Publication 118. Ann. ICRP 41(1/2).

7. NRC (National Research Council). 2006. Health Risks from Exposure to Low Levels of Ionizing Radiation. BEIR VII Phase 2. Washington, DC: National Academy Press.

8. Balter S, Hopewell JW, Miller DL, Wagner LK, Zelefsky MJ. Fluoroscopically guided interventional procedures: a review of radiation effects on patients' skin and hair. Radiology. 2010 Feb;254(2):326-41. doi: 10.1148/radiol.2542082312.

9. Douple EB, Mabuchi K, Cullings HM, Preston DL, Kodama K, Shimizu Y, Fujiwara S, Shore RE. Long-term radiation-related health effects in a unique human population: lessons learned from the atomic bomb survivors of Hiroshima and Nagasaki. Disaster Med Public Health Prep. 2011 Mar;5 Suppl 1:S122-33. doi: 10.1001/dmp.2011.21.

10. Yusuf SW, Sami S, Daher IN. Radiation-induced heart disease: a clinical update. Cardiol Res Pract. 2011 Feb 27;2011:317659. doi: 10.4061/2011/317659.

11. Dong SL, Chu TC, Lan GY, Wu TH, Lin YC, Lee JS. Characterization of high-sensitivity metal oxide semiconductor field effect transistor dosimeters system and LiF:Mg,Cu,P thermoluminescence dosimeters for use in diagnostic radiology. Appl Radiat Isot. 2002 Dec; 57(6):883-91.

12. Koivisto J, Kiljunen T, Wolff J, Kortesniemi M. Characterization of MOSFET dosimeter angular dependence in three rotational axes measured free-in-air and in soft-tissue equivalent material. J Radiat Res. 2013 Sep; 54(5):943-9. doi: 10.1093/jrr/rrt015. Epub 2013 Mar 21.

13. Pomije BD, Huh CH, Tressler MA, Hintenlang DE, Bolch WE. Comparison of angular free-in-air and tissue-equivalent phantom response measurements in p-MOSFET dosimeters. Health Phys. 2001 May;80(5):497-505.

14. Rowbottom CG, Jaffray DA. Characteristics and performance of a micro-MOSFET: an "imageable" dosimeter for image-guided radiotherapy. Med Phys. 2004 Mar;31(3):609-15.

15. Poludniowski GG. Calculation of X-ray spectra emerging from an X-ray tube. Part II. X-ray production and filtration in X-ray targets. Med Phys. 2007 Jun;34(6):2175-86.

16. Poludniowski GG, Philip ME. Calculation of X-ray spectra emerging from an X-ray tube. Part I. Electron penetration characteristics in X-ray targets. Med Phys. 2007 Jun;34(6):2164-74.

17. Poludniowski GG, Landry G, DeBlois F, Evans PM, Verhaegen F. SpekCalc: a program to calculate photon spectra from tungsten anode X-ray tubes. Phys Med Biol. 2009 Oct 7;54(19):N433-8. doi: 10.1088/0031-9155/54/19/N01. Epub 2009 Sep 1.

18. Wang C. Evaluation of Patient Effective Dose of Neurovascular Imaging Protocols of a C-arm Cone-beam CT & Estimation of Current Source Radioactivity of a Cs-137 Irradiator. Thesis. Duke University. 2015

19. Dong SL, Chu TC, Lan GY, Wu TH, Lin YC, Lee JS. Characterization of high-sensitivity metal oxide semiconductor field effect transistor dosimeters system and LiF:Mg,Cu,P thermoluminescence dosimeters for use in diagnostic radiology. Appl Radiat Isot. 2002 Dec; 57(6):883-91.

20. Pomije BD, Huh CH, Tressler MA, Hintenlang DE, Bolch WE. Comparison of angular free-in-air and tissue-equivalent phantom response measurements in p-MOSFET dosimeters. Health Phys. 2001 May;80(5):497-505.

21. Koivisto J, Kiljunen T, Wolff J, Kortesniemi M. Characterization of MOSFET dosimeter angular dependence in three rotational axes measured free-in-air and in soft-tissue equivalent material. J Radiat Res. 2013 Sep; 54(5):943-9. doi: 10.1093/jrr/rrt015. Epub 2013 Mar 21.

22. Toncheva G, Fredrickson M, Yoshizumi TT. Variation of MOSFET calibration factor as a function of dosimeter age [abstract]. Med Phys. 2010;37(6):3116.

23. Hoffman J, Kaplan S. The incidence of congenital heart disease. J Am Coll Cardiol. 2002;39:1890 –1900.

24. UNSCEAR. Effects of ionizing radiation. Report to the General Assembly of the United Nations. New York, NY; 2006.

25. International Commission on Radiological Protection. ICRP publication 85: avoidance of radiation injuries from medical interventional procedures. Ann ICRP 2001; 30/2: Publication no. 85

26. Koenig TR, Wolff D, Mettler FA, Wagner LK. Skin injuries from fluoroscopically guided procedures. Part 1. Characteristics of radiation injury. AJR 2001; 177:3–11

27. Koenig TR, Mettler FA, Wagner LK. Skin injuries from fluoroscopically guided procedures. Part 2. Review of 73 cases and recommendations for minimizing dose delivered to patient. AJR 2001; 177:13–20

28. Chida K, Saito H, Zuguchi M, et al. Does digital acquisition reduce patients' skin dose in cardiac interventional procedures? An experimental study. AJR 2004; 183:1111–1114

29. Chida K, Kagaya Y, Saito H, et al. Total entrance skin dose: an effective indicator of maximum radiation dose to the skin during percutaneous coronary intervention. AJR 2007; 189:989; [web]:W224–W227

30. Tsapaki V, Ahmed NA, AlSuwaidi JS, et al. Radiation exposure to patients during interventional procedures in 20 countries: initial IAEA project results. AJR 2009; 193:559–569

31. Chida K, Inaba Y, Saito H, et al. Radiation dose of interventional radiology system using a flat-panel detector. AJR 2009; 193:1680–1685

32. European Community Council Directive 97/43Euratom of 30 June 1997 on health protection of individuals against the dangers of ionizing radiation in relation to medical exposure. Off J. 1997;L180:22–27.

33. Fletcher DW, Miller DL, Balter S, et al. Comparison of four techniques to estimate radiation dose to skin during angiographic and interventional radiology procedures. J Vasc Interv Radiol. 2002;13:391–397.

34. US Food and Drug Administration. Avoidance of serious X-ray-induced skin injuries to patients during fluoroscopically-guided procedures. Med Bull. 1994;24:7–17.

35. Van de Putte S, Verhaegen F, Taeymans Y, et al. Correlation of patient skin doses in cardiac interventional radiology with dose-area product. Br J Radiol. 2000;73:504 –513.

36. Vaño E, Arranz L, Sastre JM, et al. Dosimetric and radiation protection considerations based on some cases of patient skin injuries in interventional cardiology. Br J Radiol. 1998;71:510 –516.

37. Chida K, Kato M, Saito H, et al. Optimizing patient radiation dose in intervention procedures. Acta Radiol 2010; 51:33–39

38. den Boer A, de Feijter PJ, Serruys PW, et al. Real-time quantification and display of skin radiation during coronary angiography and intervention. Circulation. 2001;104:1779 –1784.

39. Lobotessi H, Karoussou A, Neofotistou V, et al. Effective dose to a patient undergoing coronary angiography. Radiat Prot Dosimetry. 2001; 94:173–176.

40. Bakalyar DM, Castellani MD, Safian RD. Radiation exposure to patients undergoing diagnostic and interventional cardiac procedures. Cathet Cardiovasc Diagn. 1997;42:121–125.

41. Yoshizumi TT, Goodman PC, Frush DP, Nguyen G, Toncheva G, Sarder M, Barnes L. Validation of metal oxide semiconductor field effect transistor technology for organ dose ssessment during CT: comparison with thermoluminescent dosimetry. AJR Am J Roentgenol. 2007 May;188(5):1332-6.

42. Wang C, Nguyen G, Toncheva G, Jiang X, Ferrell A, Smith T, Yoshizumi T. Evaluation of patient effective dose of neurovascular imaging protocols for C-arm cone-beam CT. AJR Am J Roentgenol. 2014 May;202(5):1072-7. doi: 10.2214/AJR.13.11001.

43. Chambers CE, Fetterly KA, Holzer R, Lin PJ, Blankenship JC, Balter S, Laskey WK. Radiation safety program for the cardiac catheterization laboratory. Catheter Cardiovasc Interv. 2011 Mar 1;77(4):546-56. doi: 10.1002/ccd.22867. Epub 2011 Jan 19.

44. ICRP, 1996. Conversion Coefficients for use in Radiological Protection against External Radiation. ICRP Publication 74. Ann. ICRP 26 (3-4).

45. ICRP, 2007. The 2007 Recommendations of the International Commission on Radiological Protection. ICRP Publication 103. Ann ICRP 2007;37(24):1-332.

46. Committee to Assess Health Risks from Exposure to Low Levels of Ionizing Radiation, Nuclear and Radiation Studies Board, Division on Earth and Life Studies, National Research Council of the National Academies. Health risks from exposure to low levels of ionizing radiation: BEIR VII Phase 2. Washington, DC: National Academies Press; 2006.

47. Chan HP, Lam KL, Wu Y. Studies of performance of antiscatter grids in digital radiography: effect on signal-to-noise ratio. Med Phys. 1990;17(4):655–64.

48. Gislason AJ, Davies AG, Cowen AR. Dose optimization in pediatric cardiac X-ray imaging. Med Phys. 2010 Oct;37(10):5258-69.

49. Ubeda C, Vano E, Gonzalez L, Miranda P. Influence of the antiscatter grid on dose and image quality in pediatric interventional cardiology X-ray systems. Catheter Cardiovasc Interv. 2013 Jul 1;82(1):51-7. doi: 10.1002/ccd.24602. Epub 2013 Feb 12.

50. Partridge J, McGahan G, Causton S, Bowers M, Mason M, Dalby M, Mitchell A. Radiation dose reduction without compromise of image quality in cardiac angiography and intervention with the use of a flat panel detector without an antiscatter grid. Heart. 2006 Apr;92(4):507-10. Epub 2005 Sep 13.

51. Wu G, Mainprize JG, Boone JM, Yaffe MJ. Evaluation of scatter effects on image quality for breast tomosynthesis. Med Phys. 2009;36(10):4425–32.

52. Veldkamp WJ, Thijssen MAO, Karssemeijer N. The value of scatter removal by a grid in full field digital mammography. Med Phys. 2003;30(7):1712–18.

53. Neitzel U. Grids or air gaps for scatter reduction in digital radiography: a model calculation. Med Phys. 1992;19(2):475–81.

54. Gennaro G, Katz L, Souchay H, Klausz R, Alberelli C, di Maggio C. Grid removal and impact on population dose in full-field digital mammography Med Phys. 2007;34(2):547–55.

55. Patton, Kevin T., and Gary A. Thibodeau. Anatomy & Physiology. St. Louis, MO: Mosby/Elsevier, 2010. Print.

56. ICRP, 2002. Basic Anatomical and Physiological Data for Use in Radiological Protection Reference Values. ICRP Publication 89. Ann. ICRP 32 (3-4).

57. Fujii K, Akahane K, Miyazaki O, Horiuchi T, Shimada A, Nagmatsu H, Yamauchi M, YamauchiKawaura C, Kawasaki T. Evaluation of organ doses in CT examinations with an infant anthropomorphic phantom. Radiat Prot Dosimetry 2011; 147:151-155

58. Wang C, Nguyen G, Toncheva G, Jiang X, Ferrell A, Smith T, Yoshizumi T. Evaluation of patient effective dose of neurovascular imaging protocols for C-arm cone-beam CT. AJR Am J Roentgenol. 2014 May;202(5):1072-7.

59. Shin R, Cabrera F, Nguyen G, Wang C, Chung YH, Yaacoub R, Scales C, Ferrandino M, Preminger G, Yoshizumi TT, Lipkin M. Increased radiation dose rate during ureteroscopy in the obese patient. J Endourol. 2015 Sep 28.

60. Yoshizumi TT, Goodman PC, Frush DP, Nguyen G, Toncheva G, Sarder M, Barnes L. Validation of metal oxide semiconductor field effect transistor technology for organ dose assessment during CT: comparison with thermoluminescent dosimetry. AJR Am J Roentgenol. 2007 May;188(5):1332-6.

61. Chan HP, Lam KL, Wu Y. Studies of performance of antiscatter grids in digital radiography: effect on signal-to-noise ratio. Med Phys. 1990;17(4):655–64.

62. Gislason AJ, Davies AG, Cowen AR. Dose optimization in pediatric cardiac X-ray imaging. Med Phys. 2010 Oct;37(10):5258-69.

63. Ubeda C, Vano E, Gonzalez L, Miranda P. Influence of the antiscatter grid on dose and image quality in pediatric interventional cardiology X-ray systems.

Catheter Cardiovasc Interv. 2013 Jul 1;82(1):51-7. doi: 10.1002/ccd.24602. Epub 2013 Feb 12.

64. Partridge J, McGahan G, Causton S, Bowers M, Mason M, Dalby M, Mitchell A. Radiation dose reduction without compromise of image quality in cardiac angiography and intervention with the use of a flat panel detector without an antiscatter grid. Heart. 2006 Apr;92(4):507-10. Epub 2005 Sep.

65. Wu G, Mainprize JG, Boone JM, Yaffe MJ. Evaluation of scatter effects on image quality for breast tomosynthesis. Med Phys. 2009;36(10):4425–32.

66. Veldkamp WJ, Thijssen MAO, Karssemeijer N. The value of scatter removal by a grid in full field digital mammography. Med Phys. 2003;30(7):1712–18.

67. Gennaro G, Katz L, Souchay H, Klausz R, Alberelli C, di Maggio C. Grid removal and impact on population dose in full-field digital mammography Med Phys. 2007;34(2):547–55.

68. Neitzel U. Grids or air gaps for scatter reduction in digital radiography: a model calculation. Med Phys. 1992;19(2):475–81.

69. AAPM, "The Measurement, reporting, and management of radiation dose in CT," AAPM Report No. 96 (2008).

70. Pantos I, Patatoukas G, Katritsis DG, Efstathopoulos E. Patient radiation doses in interventional cardiology procedures. Curr Cardiol Rev. 2009 Jan;5(1):1-11. doi: 10.2174/157340309787048059.

71. Lai P1, McNeil SM, Gordon CL, Connolly BL. Lai P1, McNeil SM, Gordon CL, Connolly BL. AJR Am J Roentgenol. 2014 Dec;203(6):1336-44. doi: 10.2214/AJR.13.11445.

72. Rogers DW, Kawrakow I, Seuntjens JP, Walters BR, Mainegra-Hing E. Ottawa, ON: National Research Council of Canada; 2010. NRC User Codes for EGSnrc. NRCC Report PIRS-702 (revB)

73. Kawrakow I, Seuntjens JP, Rogers DW, Tessier F, Walters BR. Ottawa, ON: National Research Council of Canada; 2010. [Last accessed on 2013 May 15]. The EGSnrc Code System: Monte Carlo simulation of electron and photon transport. NRCC Report PIRS-701.

74. Beels L, Bacher K, De Wolf D, Werbrouck J, Thierens H. gamma-H2AX foci as a biomarker for patient X-ray exposure in pediatric cardiac catheterization: are we underestimating radiation risks? Circulation 2009;120(19):1903-9.

75. Brady, SL. Development of Radiochromic Film for Spatially Quantitative Dosimetric Analysis of Indirect Ionizing Radiation Fields. Thesis. Duke University. 2010

Biography

Chu Wang was born in Liaoyang, a small city in northeastern China in 1987. Chu completed his M.S. in Medical Physics at Duke University in 2012 and his B.S. in Medical and Health Physics at McMaster University in 2010. His research interests lie in the area of radiation dosimetry, radiation-associated health effects and radiation protection. Since joining the Duke Radiation Dosimetry Laboratory as a graduate student, his research has focused on radiation dosimetry in medical imaging and radiobiological research. Following these interests, Chu has published articles on various scientific journals such as the American Journal of Roentgenology, Journal of Health Physics and Journal of Medical Physics. Chu was awarded the Health Physics Society Fellowship in 2013 and is currently an active student member of the Health Physics Society.

Chu is a co-founder of Golden Horseshoe Education Corp. (GHEC), an education consulting firm based in Ontario, Canada. As GHEC's senior education consultant, his clienteles include both students and education institutions in international education and cultural exchange programs, for whom he provides consultations to improve the quality of education to individuals as well as the overall effectiveness in program management.

Outside of his work in science and education, Chu is an avid student in world history, economics, arts and literature.